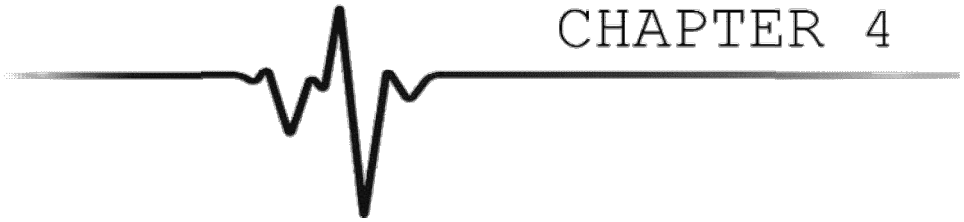

CHAPTER 4

CHAPTER 4

GEOMETRY OF MOHO AND THE MAIN HIMALAYAN THRUST

4.1. INTRODUCTION

The investigation of the shear wave velocity structure of both crust and upper mantle provides important information regarding the geodynamics and seismogenesis of a region. The variations in fundamental properties such as crustal thickness, shear wave velocities at different depths, and Poisson's ratio are interpretable in terms of processes that are associated with evolution and modification of the subsurface configuration. The collision and the subsequent underthrusting of the Indian plate underneath Asia resulted in large lateral variations in crustal thickness and its composition. Several geophysical experiments like INDEPTH (in three different phases- I, II and III) and Hi-CLIMB in Tibetan Plateau (e.g. Nelson et al., 1996; Schulte-Pelkum et al.,2005; Nabelek et al., 2009) and HIMPROBE in the NW Himalaya (Gokarn et al., 2002; Jain et al., 2003; Rai et al., 2006) have been carried out to understand the configuration of crust. The HIMPROBE experiment covered a few transects across the NW Himalaya, however, a large part of the NW Himalaya has not been explored by any geophysical experiment. Few recent studies (Rai et al., 2006; Oreshin et al., 2008, 2011; Hazarika et al., 2013; 2014) have reported northward deepening of the Indian Moho from ~40 km below the Himalayan foredeep to ~75-80 km beneath Ladakh - Karakoram region. Besides the study of Moho depth variations, few seismological (Caldwell et al., 2009; Hazarika et al., 2014) as well as Magnetotelluric (Arora et al., 2007; Rawat et al., 2014) studies reveal the presence of partial melts or aqueous fluids at mid-crustal depths in the NW Himalaya. Despite these studies, most part of the NW Himalaya, particularly the Satluj valley region is

largely unexplored by any geophysical studies to understand the nature of intra-crustal features like the MHT. A large amount of strain energy accumulates in the MHT due to the India-Asia collision and is released from time to time by large/great earthquakes (Bilham et al., 1995; Pandey et al., 1995; Larson et al., 1999). Hence investigation of the nature and geometry of the MHT is important to understand the seismicity of any region.

In this chapter, an attempt has been made to image the subsurface crust-mantle structures as well as intra-crustal features beneath the Satluj valley region. Teleseismic waveform data recorded by 18 BBS stations installed in the study region were analyzed using RF method. Shear wave velocity models are obtained at each station by inverting RF data using NA. Finally, the CCP migration method has been adopted to obtain the along-profile variation of the crustal structure.

4.2. DATA SELECTION

The teleseismic data used for RF computation are obtained from 18 BBS stations installed in the study area (Fig. 4.1). The locations of these seismological stations and the instruments used at each station are described in Chapter 3. More than 3000 teleseismic earthquake waveform data obtained from these 18 BBS stations with an epicentral distance range of Δ: 30^{o}-90^{o} having body-wave magnitude ($M_b \geq 5.5$ were selected based on higher SNR. The hypocentral information and magnitude of the selected earthquakes were extracted from the earthquake catalog of USGS (http://neic.usgs.gov). Total 200 teleseismic earthquakes were selected occurred during 2008–2010 from 9 BBS stations of the USAT network. Total 150 earthquakes were selected from the BHAG, RMGR and CKKN stations of the LSAT network recorded during 2014-2015. Nearly 300 teleseismic earthquakes were selected from rest of the station of the LSAT network (GARH, KGHT, SADH, DIGA, RMPR, and TAPR) recorded during June 2013– May 2015.

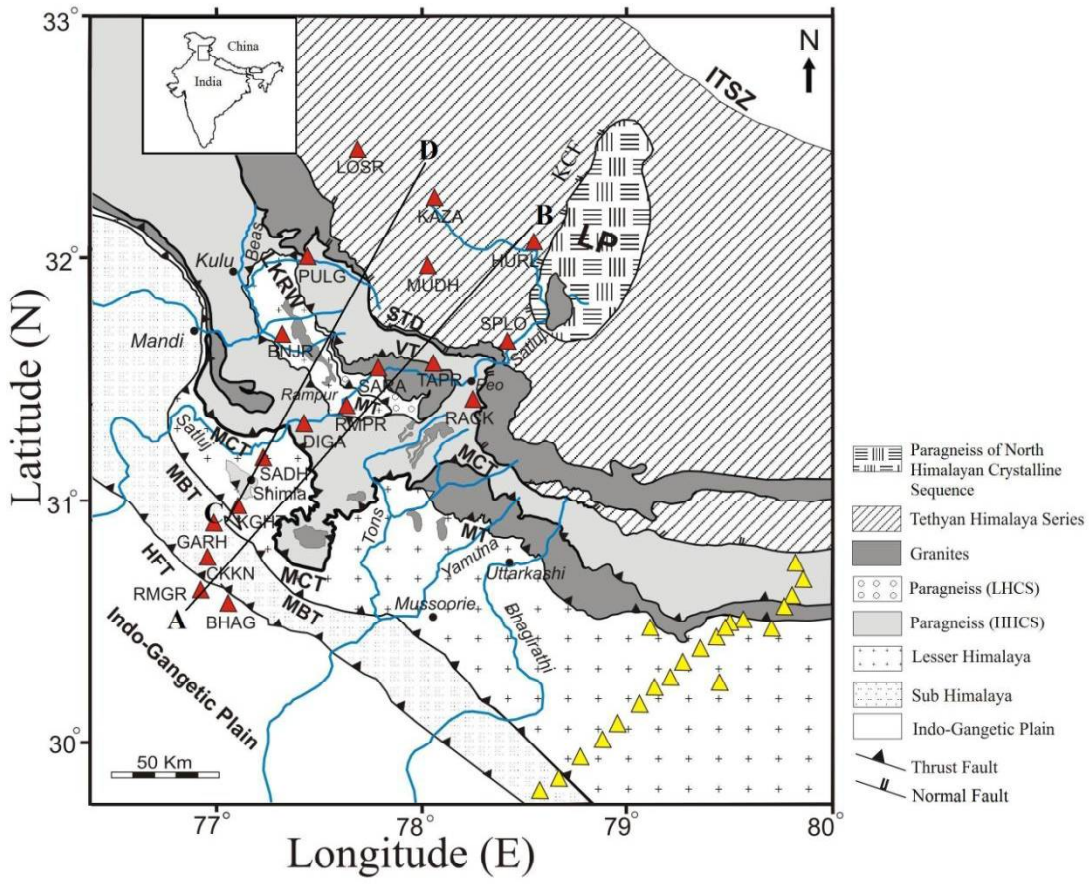

Figure 4.1 Location of spatial distribution of BBS stations installed in the area. Red and yellow triangles represent BBS stations of the present study and stations used by Caldwell et al., (2013), respectively. The line marked as AB and CD shows two profiles along which CCP stacking were performed.

The epicentral distribution of the selected earthquakes is shown in Figure 4.2. It has been observed that most of the earthquakes are from Circum-Pacific belt. Few earthquakes arriving from the northwest and southwest BAZ were also recorded and this facilitates the study of azimuthal variations of the crustal structure beneath the region.

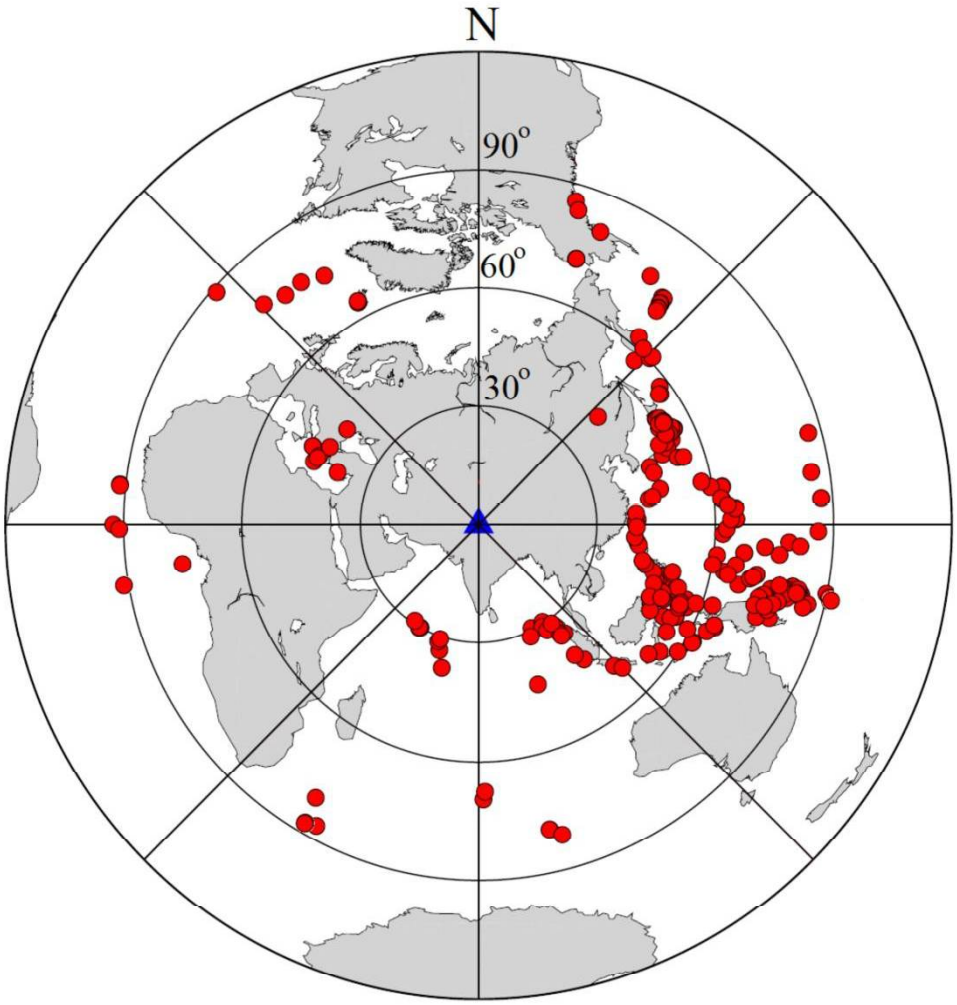

Figure 4.2 Red marked circles showing the spatial distribution of 300 teleseismic earthquakes having body wave magnitude (Mb) > 5.5 and epicentral distance of 30°-90°, considered for RF analysis for the current study. Blue triangle at the centre shows network centre.

4.3. DATA ANALYSIS AND RESULTS

4.3.1. RF COMPUTATION AND RECOGNITION OF PHASES

The RFs are computed following the deconvolution method proposed by Ligorria and Ammon, (1999). Prior to the deconvolution, teleseismic waveforms are pre-processed as described in chapter 2. A total of 100 iterations have been carried out in each deconvolution step. The RFs with high SNR and 80 % waveform fit in the deconvolution process are selected for further analysis.

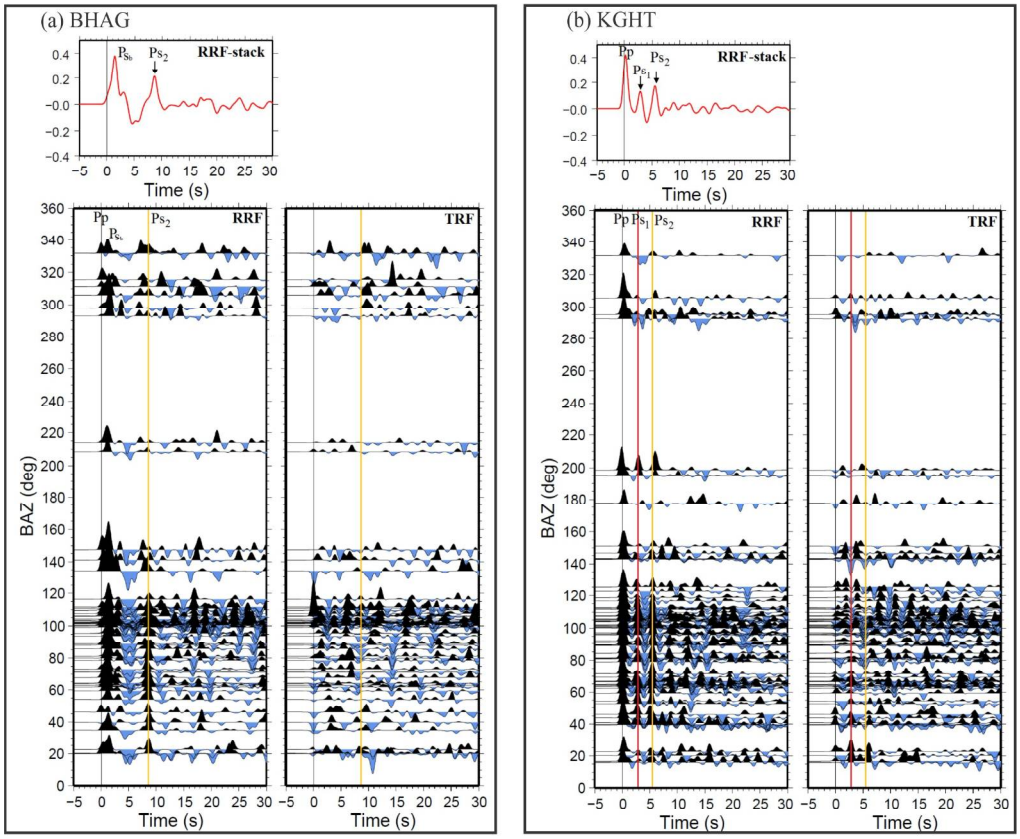

Figure 4.3 Radial and tangential RFs as a function of BAZ at (a) BHAG and (b) KGHT. The upper panel shows corresponding stacked RFs of radial component (RRF-stack).

To portray the adopted method, the RF analyses at BHAG and KGHT stations are described as follows. Selected RRFs and TRFs are plotted as a function of BAZ (Fig. 4.3). The BHAG station recorded 150 teleseismic earthquakes out of which the RFs computed from 59 best-selected earthquakes arriving from a wide range of BAZ (20^{o}-330^{o}) are shown in Figure 4.3*a*. The RRFs shows typical characteristics at this station where first *P*-arrival (i.e. *Pp* phase) is not observed at 0 s. Instead, a positive arrival at ~ 2.0 s is observed which is followed by another strong positive arrival within 3.0-3.5 s (Fig. 4.3*a*). A pair of negative arrival is observed at ~ 4.0-6.0 s. After these negative arrivals, a strong and positive arrival is detected at ~7.7 s consistently from all BAZ. Based on the arrival time and polarity, this phase is considered as the Moho-converted *Ps* phase.

In order to understand the wiggles of the RF, a synthetic test has been conducted. The results of the synthetic tests are depicted in Figure 4.4. The

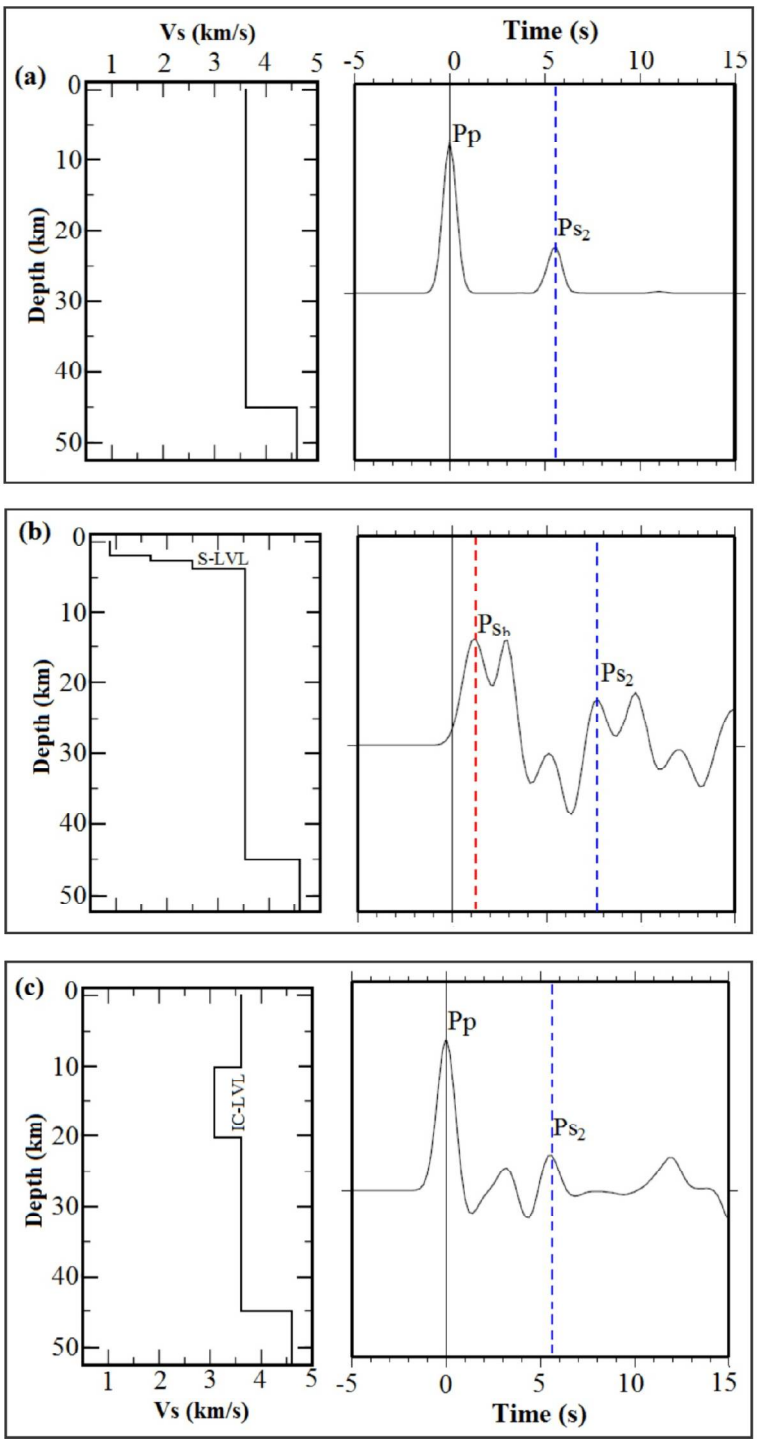

Figure 4.4 Synthetic RFs corresponding to (a) simple velocity model, (b) model with surface low-velocity layer (S-LVL) and (c) with intra-crustal low-velocity layer (IC-LVL).

propagator matrix method of Kennett, (1983) has been adopted. Initially, a simple *S*-wave velocity (*Vs*) model with average *Vs* of 3.6 km/s for 45 km thick crust has been considered for the generation of synthetic RF. The synthetic RF shows *Pp* phase at 0 s and a strong positive arrival at ~5.5 s, considered as *Ps* phase (Fig. 4.4*a*). In the second synthetic test, low *Vs* (< 1 km/s) at the top 3-4 km thick sedimentary crust is introduced. This modified model produces synthetic RF comparable with the observed RFs of the BHAG station. The *Pp* phase, as observed in the first test, disappears at 0 s, instead, a positive phase doublet appeared within 1.2-3.0 s and Moho converted *Ps* phases shifted to ~7.5 s (Fig. 4.4*b*). The positive arrival observed at ~1.2-3.0 s can be considered as *P*-to-*S* converted phase (Ps_b) originated at the bottom of the sedimentary layer. This observation is a distinctive characteristic of the RFs at stations over alluviums of the IGP (Hetényi et al., 2006; Borah et al., 2015) and in other sedimentary basins (e.g. Zelt & Ellis, 1999; Hazarika et al., 2012; Yeck et al., 2013; Saikia et al., 2017).

On the contrary, direct *P*-wave arrival is observed at 0 s in the RRFs observed at KGHT, followed by negative arrivals at ~2.0 s and ~4.0 s and two significant positive arrivals at ~2.6 s and 5.5 s (Fig. 4.3*b*). A total of 300 teleseismic earthquakes have been analyzed for KGHT however best 170 RFs were selected based on high SNR. A negative phase arrival is observed in the RRFs at ~2.0 s. This phase indicates the presence of an intra-crustal low-velocity layer (IC-LVL). The negative phase can originate at top of the IC-LVL. This phase is however, insignificant or weak in some RRFs. The positive arrival marked by Ps_1 at ~2.6 s represents a shallow interface and thus it cannot be the Moho discontinuity. This phase may correspond to a converted phase originated at the bottom of the IC-LVL coinciding with the MHT. Depending up on the polarity and comparing arrival time with previous studies (e.g. Rai et al., 2006; Oreshin et al., 2008, 2011), the second positive arrival (Ps_2) detected at ~5.5 s, can be inferred as Moho converted *Ps* phase. The characteristic features of RFs at KGHT station is similar to the third case of the synthetic test (Fig. 4.4*c*), where an IC-LVZ is introduced in the simple model (Fig. 4.4*a*). The characteristic waveforms due to an IC-LVL show

negative amplitude peaks. In addition to the RFs of BHAG and KGHT, examples of RRFs computed at rest of the stations are shown in Figure 4.5. The RF for other stations were also computed and interpreted in the same way.

4.3.2. RF ALONG THE TRANSECT

RF computed at each station show characteristics features of the individual recording site. In order to inspect azimuthal variation in crustal structure beneath a recording site, the RFs of teleseismic earthquakes coming from different back azimuths were plotted as a function of BAZ for each recording station and these are depicted in Figures 4.3 and 4.5. The prominent first positive arrival observed at 0 s at most of the stations is the direct *P* or *Pp* phase. This phase is, either, weak or missing for stations located over the IGP (e.g. BHAG and RMGR) and the Siwalik Himalaya (e.g. CKKN). On the other hand, a positive arrival has been observed at ~1.5 s from all BAZ followed by another positive arrival within 2.0-2.5 s forming a phase doublet. These phase doublets originate due to sedimentary basin of the IGP. Similar observations have also been reported in sedimentary basins elsewhere (Hetényi et al., 2006; Hazarika et al., 2012; Yeck et al., 2013; Borah et al., 2015). The negative arrivals have been observed at ~ 4.0 s which is the multiples of *Pp* phase in the sedimentary column. The strong positive arrivals observed within 7.0-8.0 s at these stations has been considered as the Moho converted *Ps* phase. The GARH station also shows similar characteristics where the first positive arrival has been observed at 0.5 s instead of 0 s. This phase is followed by a negative phase at 1.5 s and two prominent positive arrivals at 3.0 s and 6.5 s (Fig. 4.5*c*). Similar to previous studies conducted by Rai et al. (2006), Oreshin et al. (2008) and Hazarika et al. (2013, 2014) in close proximity to the current study profile, the positive arrivals, both at ~3.0 s at the mid-crustal layer (Ps_1) and ~6.5 s at the Moho discontinuity (Ps_2), are inferred as converted phases.On the contrary to the above stations, the KGHT, SADH, DIGA, BNJR, and TAPR stations show the *Pp* phases at 0 s followed by Ps_1 and Ps_2 at 2.5-4.0 s and 5.0-6.0 s, respectively from all BAZ (Figs. 4.3 and 4.5). The RMPR station, on the other hand, shows Ps_1 phase at 3.5 s for the earthquakes coming from the northwest and southeast only, whereas Ps_2

phase is observed at 5.0 s from all BAZ. The SARA station shows strong azimuthal variations of Ps_1 and Ps_2 phases. For almost all RFs of BAZ, the Ps_1 phase is detected at 3.5 s. The Ps_2 phase is observed at 6.0 s only for

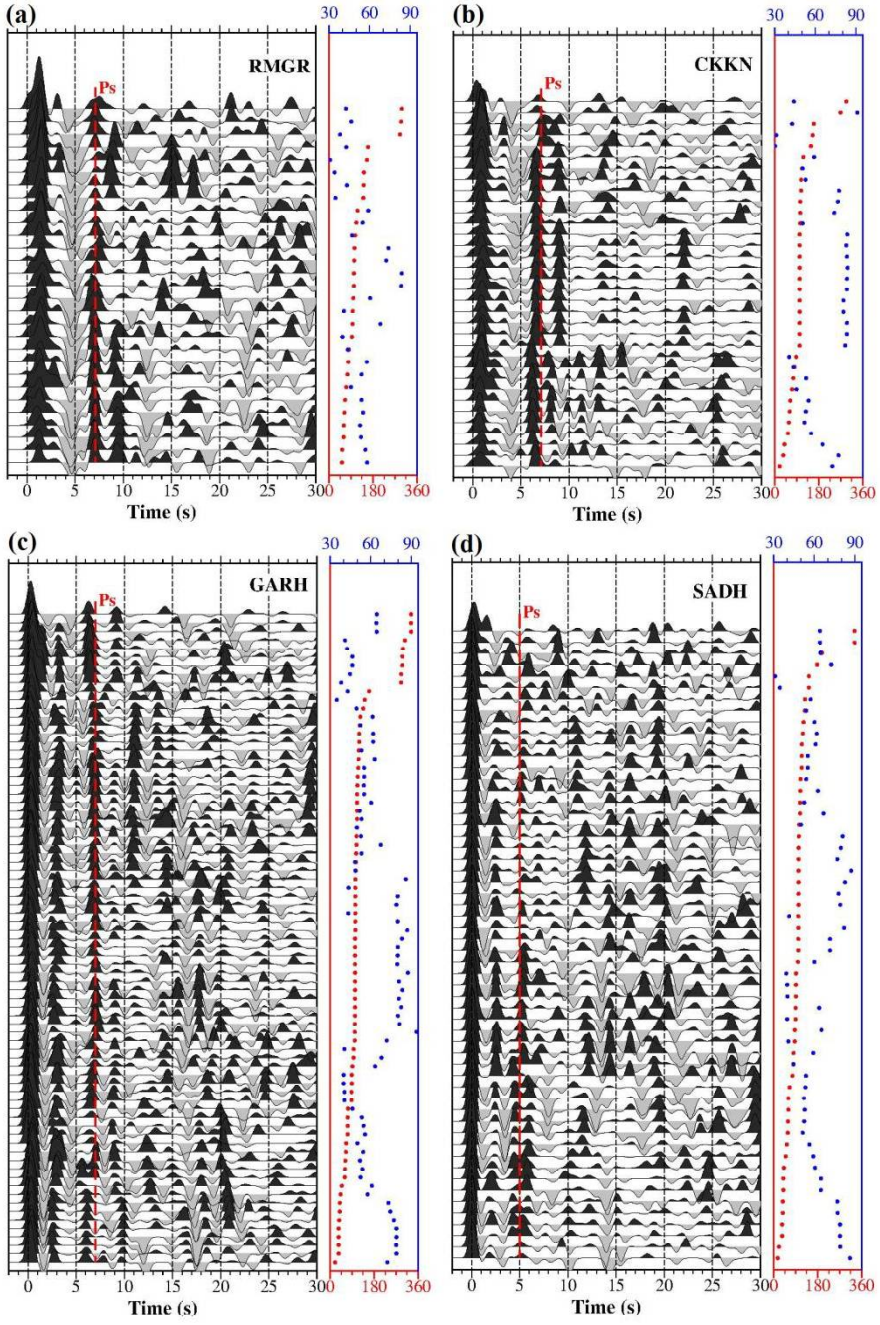

Figure 4.5 RRFs of (a) RMGR, (b) CKKN, (c) GARH (d) SADH stations in increasing back azimuth plotted with equal spacing. Station code is shown at the top right corner of each plot. The right panel at each station shows BAZ (red dots) and Δ (blue dots) corresponding to the individual RRFs.

earthquakes arriving from the northeast and northwest BAZ. This observation suggests wide variation in azimuth of crustal structure. The RFs computed at PULG and RACK stations show Ps_2phases at 6.5 s and 7.0 s, respectively consistently from all BAZ. The Ps_1 phases are observed at 2.5 s and 4.0 s, respectively for earthquakes from the southeast BAZ. The SPLO station shows

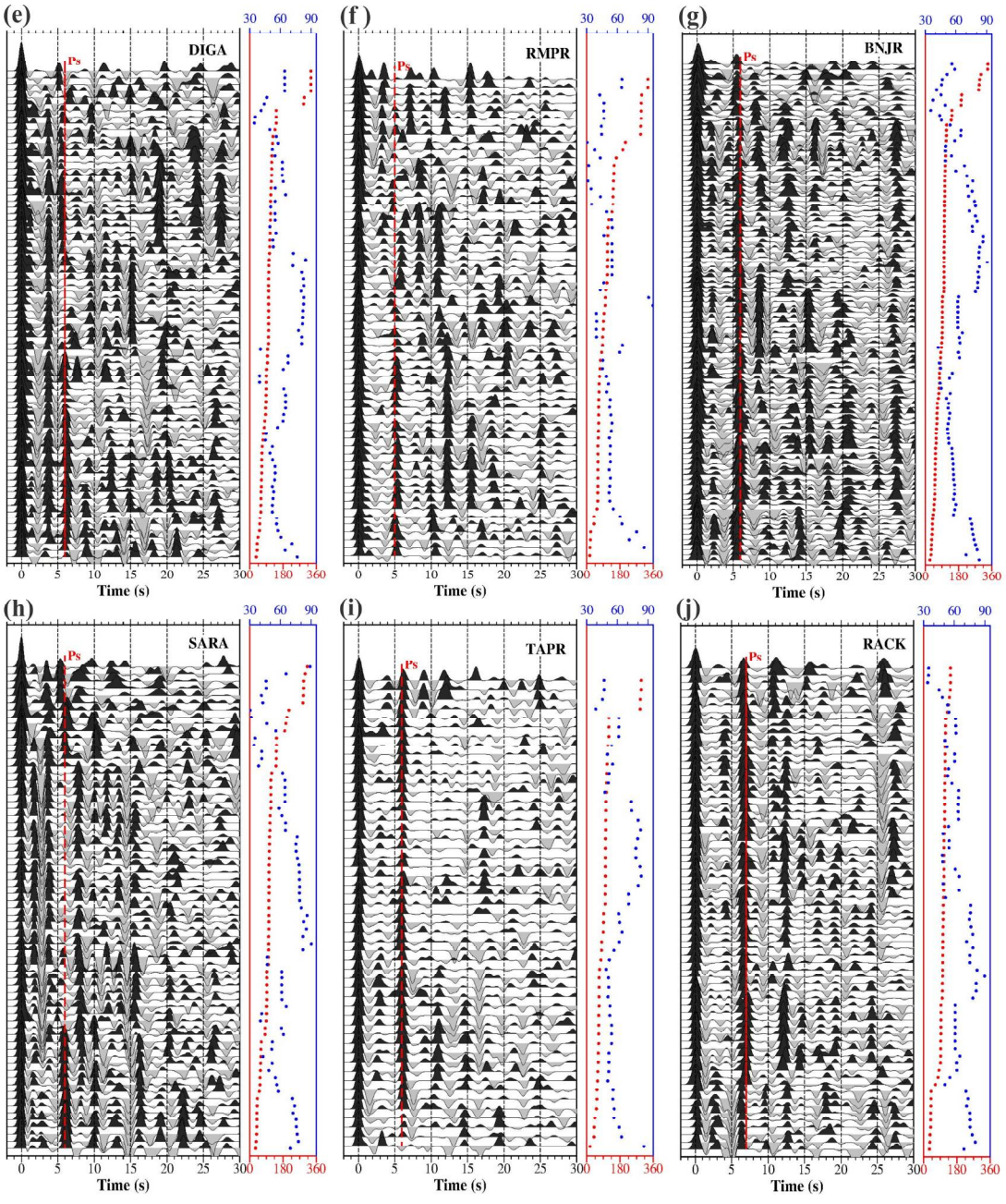

Figure 4.5 (continued) RRFs of (e) DIGA, (f) RMPR, (g) BNJR, (h) SARA, (i) TAPR, and (j) RACK

Ps_1 and Ps_2 phases consistently at ~3.5 s and 6.5 s, respectively. The MUDH, LOSR, and KAZA stations located in the TH show two positive arrivals prior to Ps_2 phase (Fig. 4.5). The positive arrival at ~4.0-5.0 s is recognized as the MHT, as the earlier positive arrival at ~2.0-3.0 s would imply shallower feature. The RFs at the HURL station (Fig. 4.5*p*) show $Ps_1$and Ps_2 at 6.0 s and 7.5 s, respectively consistently from all BAZ. A significant energy is observed in TRFs at most of the stations near the arrival time of Ps_1 and Ps_2 phases which may be due to the presence of dipping layer or anisotropy.

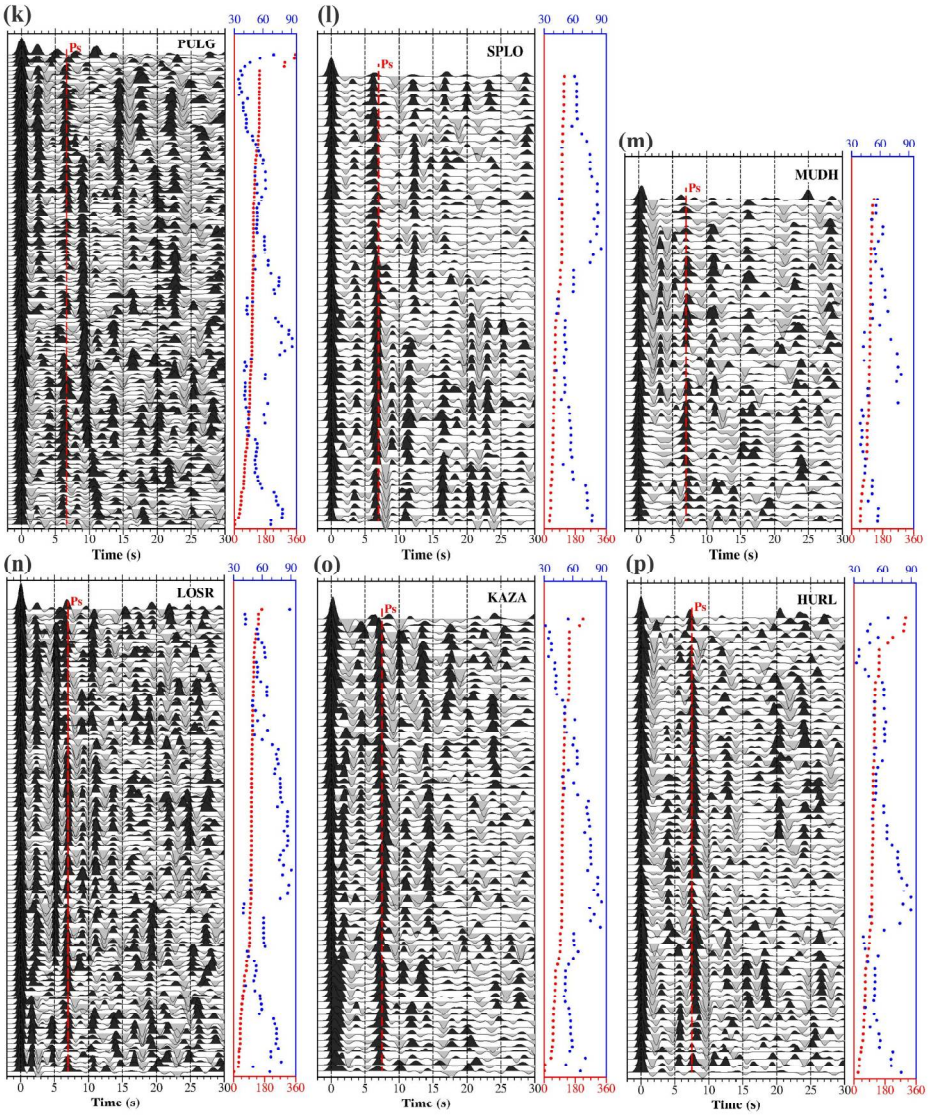

Figure 4.5 (continued) (k) PULG, (l) SPLO, (m) MUDH, (n) LOSR, (o) KAZA, and (p) HURL

4.3.3. AVERAGE CRUSTAL THICKNESS AND POISSON'S RATIO ESTIMATION

Prior to the detailed modeling of RFs, an estimate of the average thickness of the crust and Poisson's ratio are obtained by applying H-*k* stacking method of Zhu and Kanamori, (2000). The method relies on the clear record of *Ps* phase and its crustal multiple phases viz. *PpPs, PpSs* and *PsPs*. This technique has been applied to the selected RFs at GARH, KGHT, SADH, DIGA, RMPR, TAPR, RACK, SPLO, and HURL stations as shown by red triangles in Figure 4.6. The H-*k* stacking analysis for rest of the stations (e.g. BNJR, SARA, MUDH, KAZA, LOSR and PULG), shown by blue triangles, were carried out by Hazarika et al. (2013).

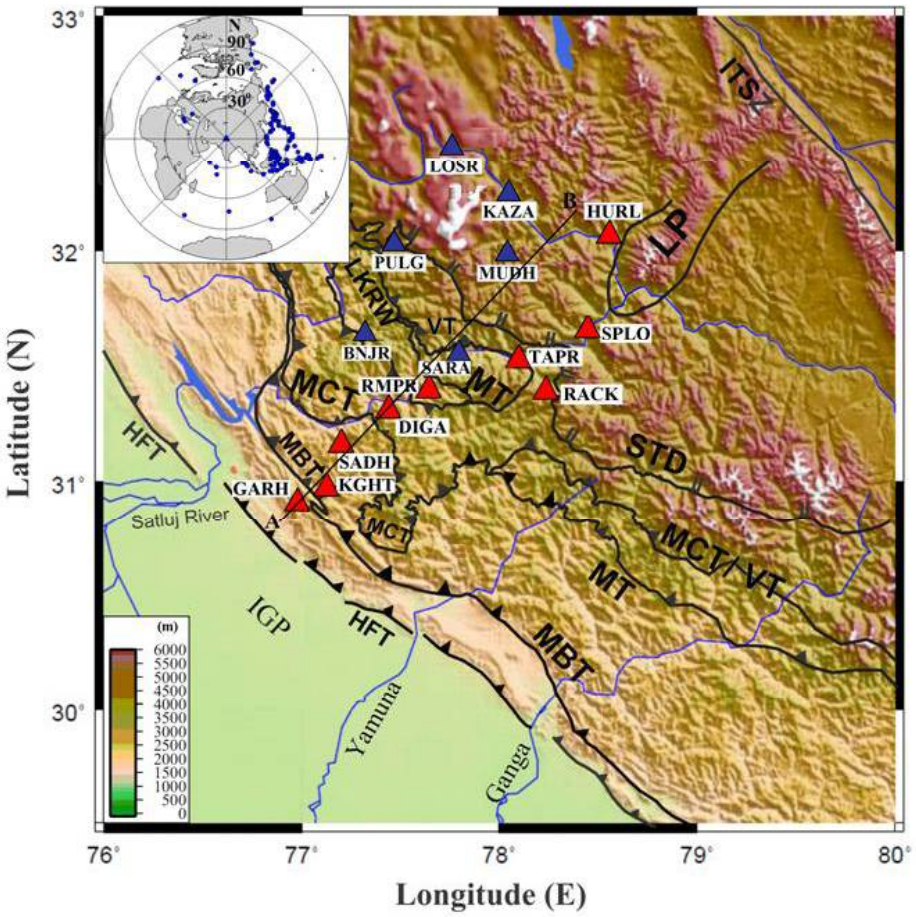

Figure 4.6 Spatial distributions of BBS stations used in H-k stacking shown by red triangles. Blue triangles indicate the BBS stations used for similar study previously by Hazarika et al. (2013).

This method needs an average value of *P*-wave velocity in the crust that can be obtained from previous geophysical study near to the study profile. Reasonable values for the average *P*-wave velocity (6.0– 6.3 km/s) obtained by previous studies (Rai et al., 2006; Borah et al., 2015) have been adopted in the H-*k* stacking analysis.

The H-*k* stack procedure is illustrated using RF data of KGHT (Fig. 4.7). Based on the clear record of Ps_1 (at ~3.0 s) and Ps_2 (at ~5.5 s) phases and

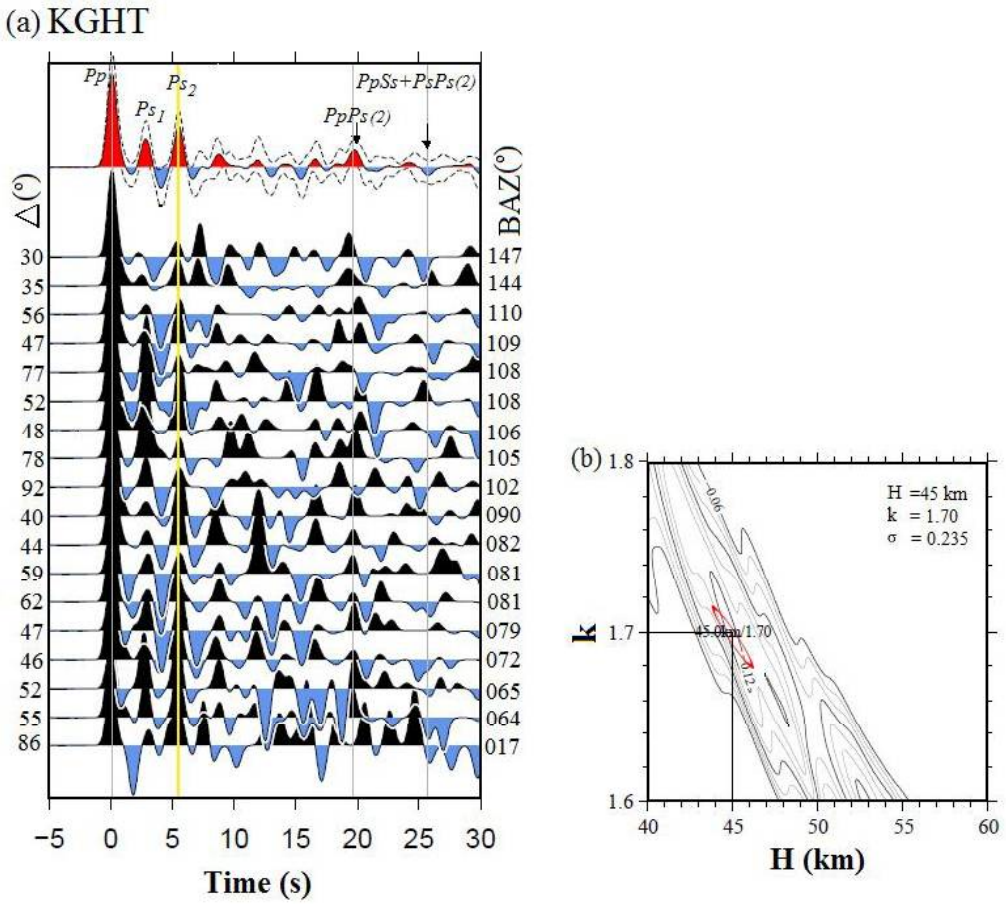

Figure 4.7 H-*k* stacking analysis at KGHT station for selected RF data. The RFs used for H-*k* stacking analysis is shown in (a) with their stack RF at the top along with + 1 SD bound computed during stacking. The Moho converted Ps2 phases is marked by yellow line and its multiples are marked by grey lines at ~19-26 s. The grey line at 0 s shows direct P arrival (Pp phase). The results of H-*k* stacking analysis using Ps2 phase and its multiples are shown in (b). The

best estimated H and *k* values are indicated by the center of the red error ellipse.

its crustal multiples (*PpPS* and *PpSS* + *PsPS* or *PpSS*), data are selected from different Δ and BAZ and plotted with their stacked RF in Figure 4.7*a*. The

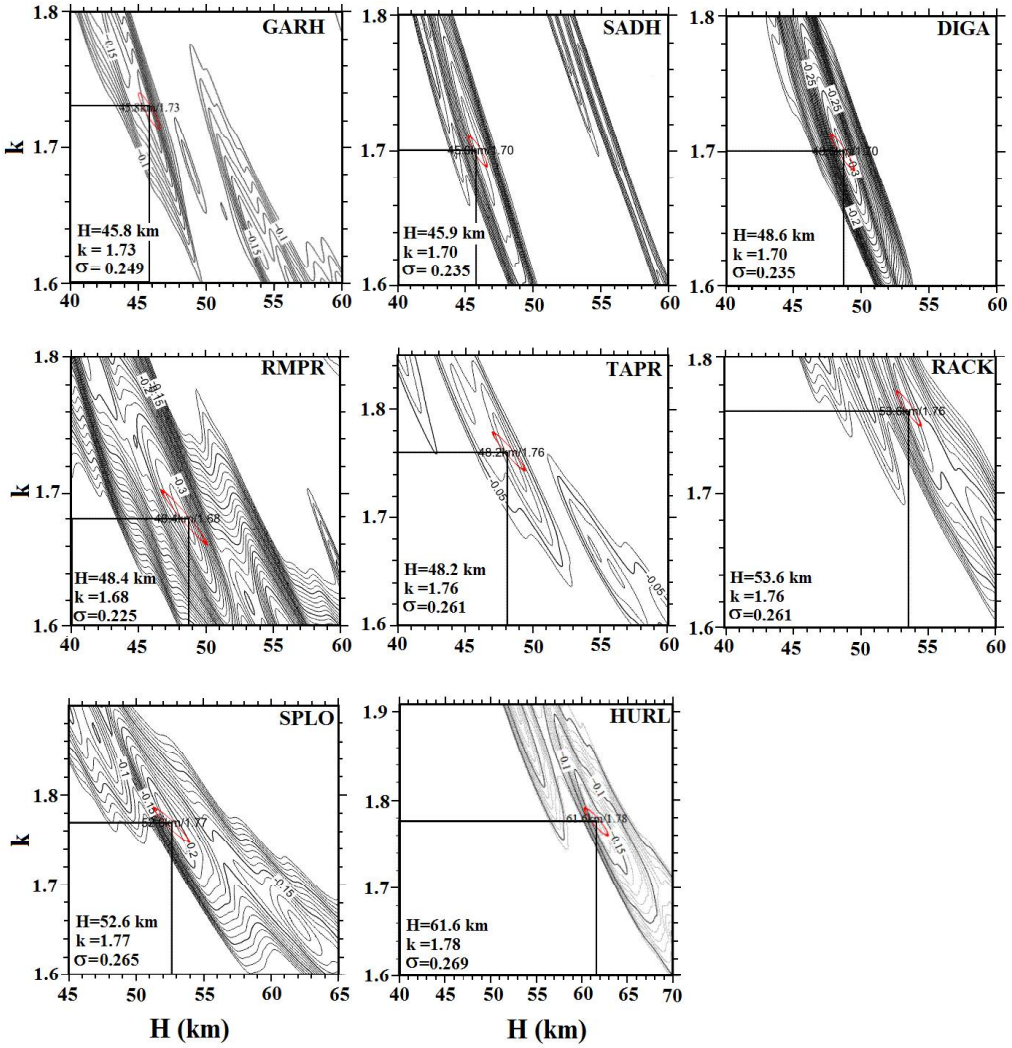

Figure 4.8 H-*k* stack results at nine stations showing *Vp/Vs* or *k* and crustal thickness (H) and their corresponding Poisson's ratio (σ) values at each station. The best estimated H and *k* values are indicated by the centre of the red error ellipse.

upper and lower SD bound computed during stacking is represented by the waveform shown by dashed lines. The RFs at KGHT show two distinct positive phases at ~ 3.0 and 5.0 s. In addition, the corresponding pairs of multiples are observed at (~9.0 s and 13.0 s) and (19.0 s and 26.0 s),

respectively. The weighting parameters are set as 0.7, 0.2, and 0.1 for converted phases and corresponding two multiple phases, respectively based on the energy of these phases. The result obtained from H-*k* stacking analysis is depicted in the form of contour plot in Figure 4.7*b*. The results show ~45 km thickness of the crust beneath KGHT with average *Vp/Vs*: 1.70 and Poisson's ratio of σ: ~0.24. The red ellipse shows error in estimation of H and *Vp/Vs* are ~0.9 km and 0.01, respectively. Following the same procedure, average crustal thickness and Poisson's ratio for GARH, SADH, DIGA, RMPR, TAPR, RACK, SPLO, and HURL stations were obtained and are depicted in Figure. 4.8. The estimated values of crustal thicknesses (H), *Vp/Vs* ratio and the corresponding Poisson's ratio (σ) is given in Table 4.1

Table 4-1 Estimated values of crustal thickness H, *Vp/Vs* ratio and the corresponding Poisson's ratio (σ) obtained for each station.

Sl. No.	Station code	Station Location			H-*k* stacking results		
		Longitude (°E)	Latitude (°N)	Elevation (m)	Average crustal thickness(H) with estimated	Average crustal Vp/Vs with estimated error	Poisson's ratio (σ)
1	GARH	76.97	30.90	1494	46±0.95	1.73±0.011	0.249
2	KGHT	77.12	30.97	1229	45±0.9	1.70±0.012	0.235
3	SADH	77.20	31.15	2111	46±0.6	1.70±0.010	0.235
4	DIGA	77.43	31.30	1979	49±1.0	1.70±0.009	0.235
5	RMPR	77.64	31.39	920	48±1.2	1.68±0.006	0.225
6	TAPR	78.09	31.52	1679	48±0.95	1.76±0.090	0.261
7	RACK	78.35	31.39	3129	54±1.0	1.76±0.010	0.261
8	SPLO	78.44	31.65	2390	53±1.2	1.77±0.010	0.265
9	HURL	78.55	32.06	3190	62±1.1	1.78±0.010	0.269

In order to depict the variations of Moho depths beneath the study profile, the estimated Moho depths from this study as well as from the study of Hazarika et al. (2013) have been projected along AB profile (Fig. 4.6). A cross-section of Moho depths and Poisson's ratios along this profile is shown in the Figure 4.9.

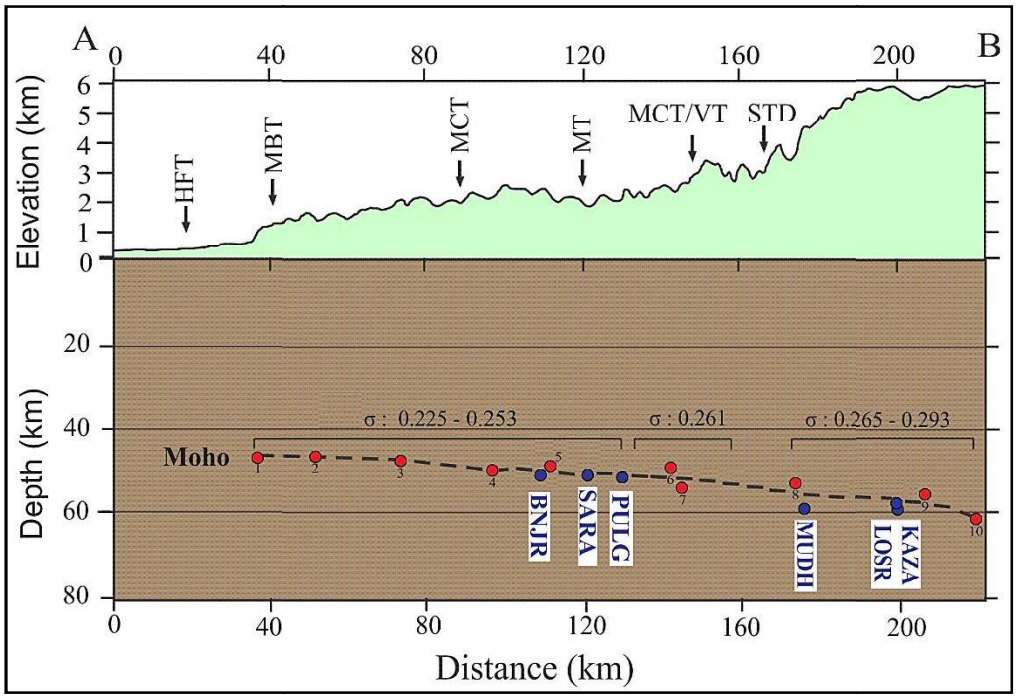

Figure 4.9 Moho crosssection through Satluj valley projected on AB profile as depicted in Figure 4.6 indicating variation in crustal thickness (H) and Poisson's ratio (σ). Red dots with serial numbers represent the obtained Moho's depth of stations as listed in Table 4.1. The blue dot represents the results at six stations obtained from previous study Hazarika et al. (2013). The range of Poisson's ratios is marked. The upper section shows the topographic variation along the AB profile of Figure 4.6.

The estimated average crustal thickness shows gentle northward dipping of Moho from ~45 km underneath the Sub-Himalaya (GARH station) to ~ 48 km underneath the Higher Himalaya (TAPR station). The crustal thickness further

in the Tethyan Himalaya. The thickening of the crust from south to north in the NW Himalaya has also beenreported by Rai et al. (2006), Hazarika et al. (2014) and Chamoli et al. (2011). A large difference in the values of Moho depth is observed between TAPR and RACK in the AB profile is due to the geographical location of the stations.

The obtained *Vp/Vs* and σ values vary significantly from south to north along the study profile. The results at the GARH shows a normal value of *Vp/Vs* (1.73) and Poisson's ratio (σ: 0.249). In general, the *Vp/Vs* and σ values are observed to be low in the Lesser Himalaya (*Vp/Vs*: 1.70; σ: 0.225), intermediate in the Higher Himalaya (*Vp/Vs*: 1.76; σ: 0.261) and high in the Tethyan Himalaya (*Vp/Vs*: 1.77-1.85; σ: 0.265-0.293). Anomalously low values of *Vp/Vs* ratio have been observed at RMPR (*Vp/Vs*: 1.68; σ: 0.225) (Wadhawan et al., 2017).

4.3.4. VELOCITY MODELS OBTAINED USING NA INVERSION

The H-*k* stacking method provides an average estimation of crustal thickness beneath a recording site; however, modeling of RFs is essential for obtaining the velocities of the shear waves at different depths. The RRFs are sensitive to crustal *S*-wave velocity. Selected RRFs with a clear record of *Ps* phases are used for inversion through NA of Sambridge, (1999*a*, *b*), described in Chapter 2. Six horizontal layers, in total, (e.g. sediment, basement, upper, middle, and lower crust, and upper mantle) are considered in the algorithm. The inversion procedure was also tested using five-layer model. The *F*-test analysis has been performed to judge the preferable number of layers and found that the six-layer model is better over the five-layer model. The *F* value was calculated from the relation given below:

$$F = \frac{\chi^2_{v_1}}{\chi^2_{v_2}}$$

$$\text{where } \chi^2_{v_k} = \frac{1}{v_k} \sum \left(\frac{d_i^{obs} - d_i^{pre}}{\sigma_i} \right)^2,$$

d_i^{obs} and d_i^{pred} are the observed and the predicted waveform, σ_i standard deviation, $v_k=N-d_k$, where N:number of data points, d:dimension of model parameter space. The length of the RFs, used here, is 25 s and sample rate: 20 SPS, thus N=500 (=25×20), and d_1=20 (=5×4) and d_2=24 (=6×4) for five-layer and six-layer models, respectively. The F value is obtained as 1.6, which is greater than the critical value of the F-distribution ($F\alpha$=1.2) for α = 0.05, thus suggesting a significant difference between the fitting for the two models and that justify the consideration of six-layer model.

Each layer is represented by layer thickness, *Vs* at top of the layer, *Vs* at bottom of the layer and *Vp/Vs* ratio. These four parameters for six different layers produce 24-dimensional parameter space used as input to NA modeling. The large parameter space helps to search best fit model from a wide range of velocity models. The gradient in a particular layer is defined by the minimum and maximum *Vs* used as input for a particular layer. These minimum and maximum *Vs* produce velocity gradients between the discontinuities. The major velocity discontinuities in the crust can be identified by velocity contrast in the inverted velocity model obtained by NA method. The minimum and maximum values of *Vs*, *Vp/Vs* ratio and the thickness of the layer are chosen in such a way that model parameterization is as flexible as possible. The advantage of NA method over least square inversion method (e.g. Ammon et al., 1990) is that this method allows a varied range of *Vp/Vs* values as input parameter during inversion. In the least square inversion technique, fixed value of Poisson's ratio (σ = 0.25) is used. A widespread range of *Vp/Vs* values within 1.60-2.65 has been used in this study. Generally, RFs with narrow epicentral distance and BAZ bins are stacked to obtain high SNR for inversion process using NA method. The RFs with epicentral distance and BAZ bins less than 20° are stacked for modeling. At some stations, where BAZ variation is insignificant, the wide range of BAZ is considered for stacking. A total of 1000 iterations were performed at each station that generates 40,020 velocity models. An objective function, which is the L_2-norm of the difference between the observed and predicted RF for a given model, is applied to estimate misfit between synthetic and observed waveforms. In order

to obtain stable inversion results, different velocity model parameterizations and incident angles are used.

To illustrate the modeling procedure, the RRF data of the KGHT station is used (Fig. 4.10*a*). An initial model necessary for the NA modeling scheme is constructed using published velocity models near the study profile (Rai et al., 2006; Mahesh et al., 2013). The inversion procedure computes synthetic RRFs corresponding to 40,020 1-D models (Fig. 4.10*b*). At each iteration, observed and synthetic RFs are compared and 1000 best fit models are selected. These best fit models are shown by colored section in Figure 4.10*b*. The best fitting and the average *Vs* are shown by the red and white lines plotted over the 1000 best models. The red lines shown at the left side of the velocity models represent estimated *Vp/Vs* ratio. The synthetic RF corresponding to best fit model is shown with ±1 SD bounds (Fig. 4.10*c*). The Moho and intra-crustal phases are marked based on the large change in velocity with depth. The Moho is marked at a depth where significant velocity gradient with *Vs* ~4.4 kms^{-1} or higher is observed. The estimated shear wave velocity model at KGHT shows slightly low *Vs* at the surface (~2.6 kms^{-1}), which increases to ~ 3.6 km s^{-1}at a depth of around 9 km. An IC-LVZ with an average *Vs*~3.2 km s^{-1} is observed at a depth range of 9-20 km. The *Vs* increases to ~3.6 kms^{-1} at a depth of ~20 km and becomes maximum (Vs ~4.39 kms^{-1}) in the lower crust. The step in velocity at ~46 km corresponding to *Ps* phase detected at ~5.5 s is believed to be the Moho discontinuity. The change in *Vs* at ~20 km is attributed to the MHT. This layer corresponds to the positive arrival at ~3.0 s. The modeling procedure illustrated for KGHT is applied for all the stations used in this study.

The shear wave velocity models obtained using NA inversion at each station are given in Figures 4.11*a*, *b* and *c*. The shear wave velocity models acquired at stations of the southern part of the study profile (e.g. BHAG, RMGR and CKKN) show surface low-velocity layer (S-LVL) with *Vs* ~0.8-1.8 km/s in the upper most 3-4 km of the crust (Fig. 4.11*a*). The inversion results show ~43-44 km thickness of the crust beneath these stations. Similar S-LVL with *Vs* ~1.0 km s^{-1} is also observed at GARH. The *Vs* increases up to ~3.5 km s^{-1} at a depth of ~4 km and then reduced to ~3.2 km s^{-1} at ~10 km

depth forming an IC-LVL. There is a considerable change in *Vs* (~3.6 kms^{-1}) at ~16 km which can produce positive arrival that corresponds to the Ps_1 phase. This layer can be attributed to the base of the IC-LVL and is marked as the MHT. The Moho depth is identified at ~45 km where there is step change in *Vs* (Fig. 4.11*a*).

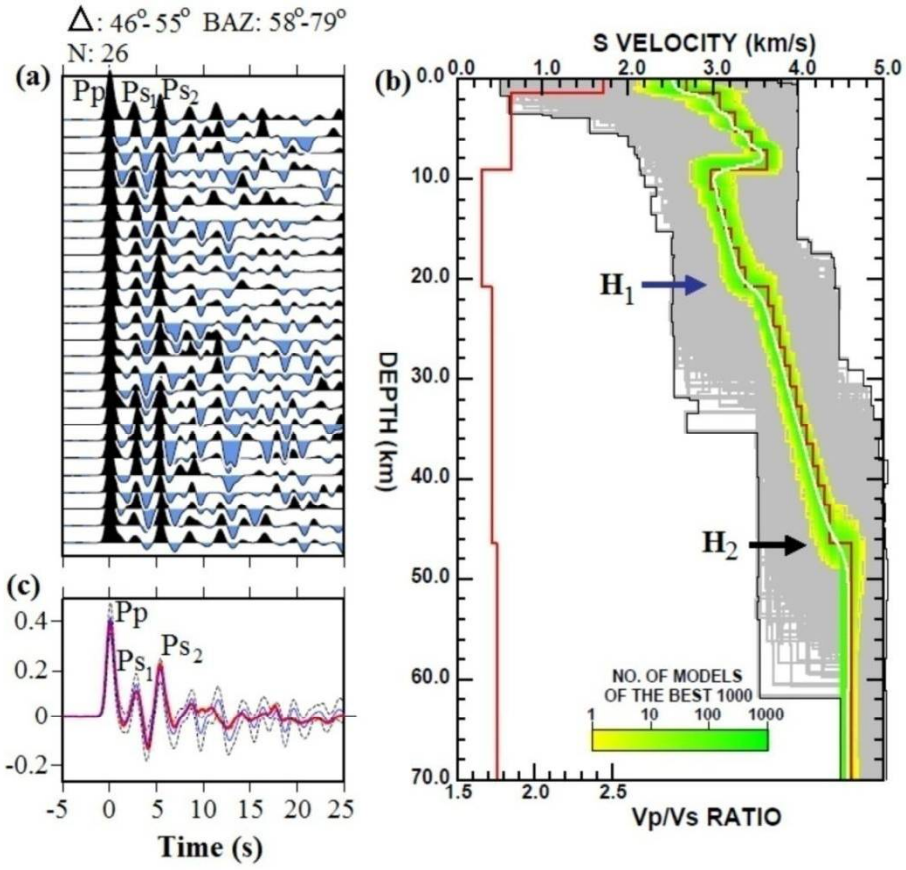

Figure 4.10 RF inversion using NA algorithm at KGHT station. (a) RRF in a narrow epicenter and BAZ range, as mentioned in the top right corner. (b) The grey area indicates the range of models (40,020 models), the green area indicates the best 1000 models with a minimum error between observed and computed RFs. The best fitting and average models are indicated by the red and white line, respectively. The best fitting Vp/Vs model (red line) is shown on the left side. The H1 and H2 are the inferred depth of the MHT and Moho discontinuity, respectively. (c) Stacked observed RF (blue

waveform) and synthetic RF (red waveform) obtained from the NA inversion with ± SD bounds (black dashed line)

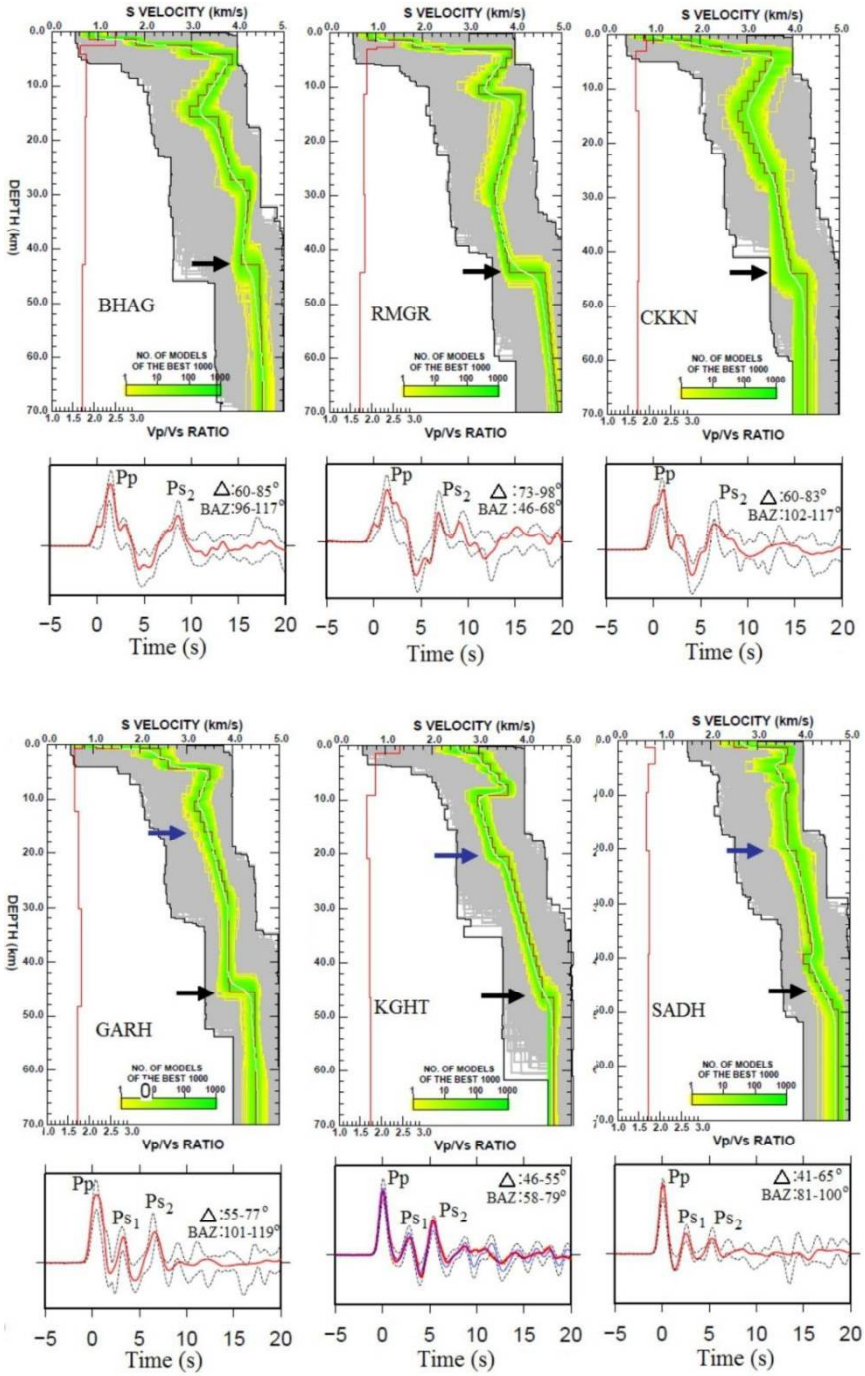

Figure 4.11*a* Shear wave velocity models acquired from NA modeling at BHAG, RMGR, CKKN, GARH, KGHT and SADH stations. The Moho and the MHT are marked by black and blue arrows respectively. Synthetic RF (red waveform) obtained from NA inversion is shown with ±1 SD bounds in lower panel at each station.

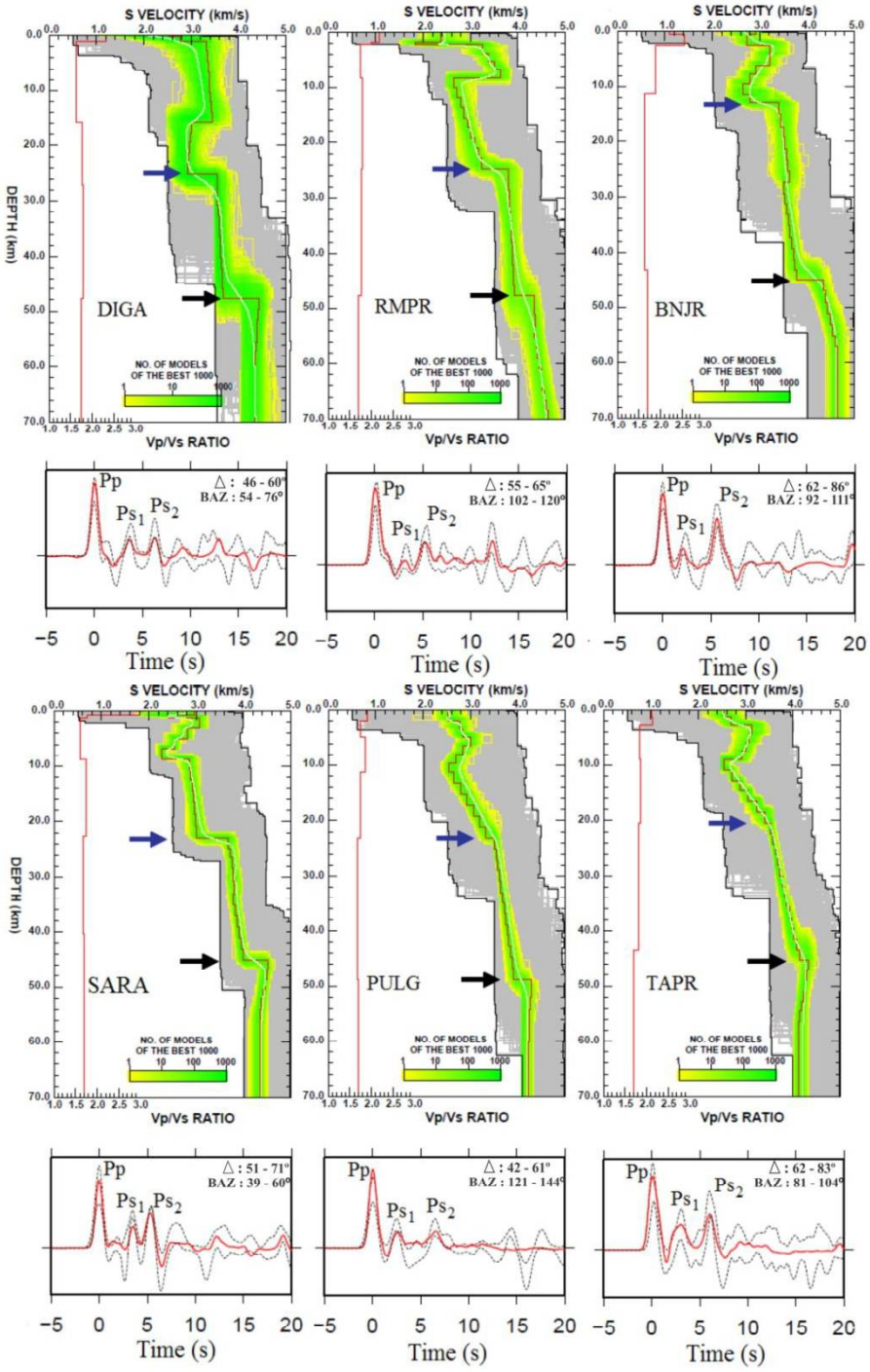

Figure 4.11*b* Shear wave velocity models acquired from NA modeling at DIGA, RMPR, BNJR, SARA, PULG and TAPR stations. The Moho and the MHT are marked by black and blue arrows, respectively.

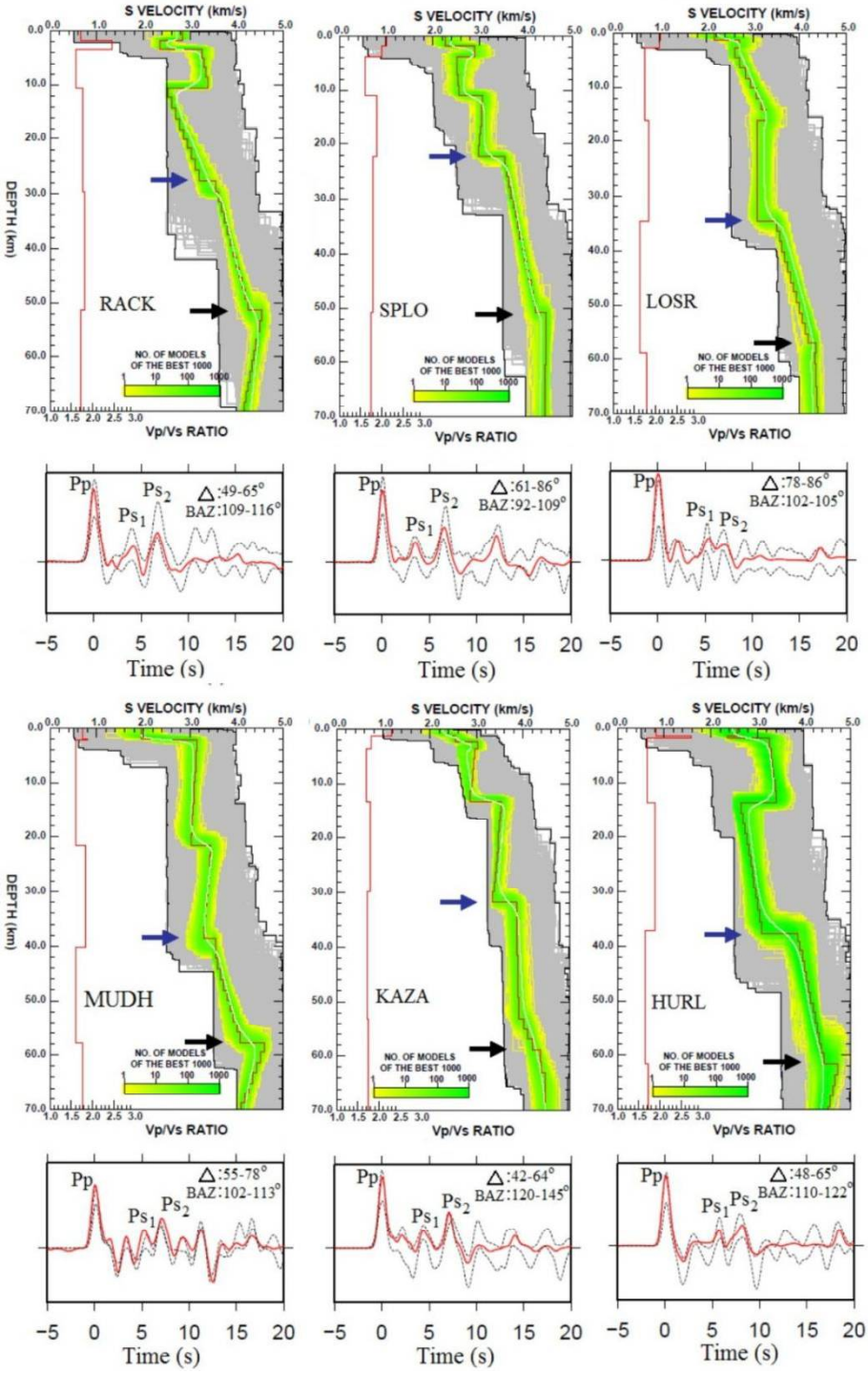

Figure 4.11*c* Shear wave velocity models acquired from NA modeling at RACK, SPLO, LOSR, MUDH, KAZA and HURL stations. The Moho and the MHT are marked by black and blue arrows, respectively.

In contrast to these stations, the S-LVL is not seen in the rest of the stations of the profile. Instead, clear IC-LVLs are observed at KGHT, DIGA, RMPR, BNJR, PULG, TAPR, RACK and HURL stations. The origin of this IC-LVL is explained in discussion section 4.4.4. At these stations, the base of the IC-LVL that produces Ps_1 is marked as the MHT (Figure 4.11*a*). At SADH station the IC-LVL is weak. In such case, a change in *Vs* at mid crust is marked as the MHT. The identification of the MHT and Moho are done in a similar way for the rest of the stations. The Moho, thus identified, is observed at ~43-44 km near the HFT which gradually increases towards north up to ~62 km in the TH (e.g. at HURL station). The depth of Moho is marked by a black arrow in the velocity models shown in Figure 4.11 whereas the depth of the MHT is marked by blue arrows. The velocity models show that the depth of the MHT varies from ~16 km underneath the Sub-Himalaya to ~27 km underneath the Higher Himalaya suggesting a gentle north dipping nature, whereas, there is a significant change in depth of the MHT beneath the Tethyan Himalaya where it attains maximum value ~38 km beneath HURL station. The RF inversion by NA method provides depths of the Moho and the MHT beneath a recording station and do not provide along-profile variation beneath the recording site. Therefore, these values are compared with image obtained from CCP migration method discussed in the following section 4.3.5.

4.3.5. COMMON CONVERSION POINT MIGRATION

The RF image is constructed by stacking of depth migrated RFs into CCP bins. The CCP stacking method is explained in Chapter 2. The CCP migrated image helps to trace variations in crustal structure, laterally, along the study profile. Initially, standard IASP91 model (Kennett & Engdahl, 1991) was used to calculate ray piercing points. Since, the Moho in the original IASP91 model is significantly shallower (35 km) than in the study area, the modified IASP91 model with Moho depth 70 km is finally used for the stations located in the northern region of HFT to construct CCP image.

The shear wave velocity model obtained from NA inversion is used for BHAG, CKKN and RMGR stations to incorporate the effect of low *S* wave

velocity observed at the surface due to the sedimentary column. Computation of the geographical distributions of ray piercing points of *P*-to-*S* conversions up to 100 km depths is carried out with a regular depth interval of one km. The travel time of *P*-to-*S* converted phases at different depths are calculated following Dueker and Sheehan, (1998). Here, the crust is considered to be composed of flat horizontal layers. The ray piercing points computed at different depths cover a considerable volume along the profile. This volume is split into several unit blocks of one km height and length and horizontally smoothed over 10 km. The amplitudes of rays passing through each block are averaged.

The CCP depth migrated RF image has been constructed along the A-B profile (Fig. 4.1) and shown in Figure 4.12. The RFs computed using two different frequencies; *Gw* 2.0 and 5.0 are used for obtaining CCP images with low and comparatively high frequencies, respectively. Data from 15 stations RMGR, BHAG, CKKN, GARH, KGHT, SADH, DIGA, RMPR, SARA, TAPR, RACK, SPLO, MUDH, KAZA, and HURL stations have been chosen for constructing the CCP image along the A-B profile (Fig. 4.12). The BNJR, PULG, and LOSR stations are not included as these are away from the A-B profile.

The ray piercing points for the BHAG and RMGR stations located in the IGP and CKKN and GARH stations of the Sub-Himalaya are calculated using the velocity model estimated by NA inversion at the BHAG station considering 3.0 km thick sedimentary layer having *Vs* ~2.2 km/s (*Vp/Vs* ~2.3) and the Moho depth at ~44 km. The ray piercing points for the other stations of the profile are calculated using the standard IASP91 model, keeping Moho depth at 70 km. The depths of Moho and the MHT, obtained from NA models, are shown by black and yellow circles, respectively. The CCP image is also obtained for other orientations, but not much significant variation is observed. A CCP image constructed along the C-D profile (Fig. 4.1) is shown in Figure 4.13. The CCP image along the C-D profile also shows similar features as observed in the A-B profile.

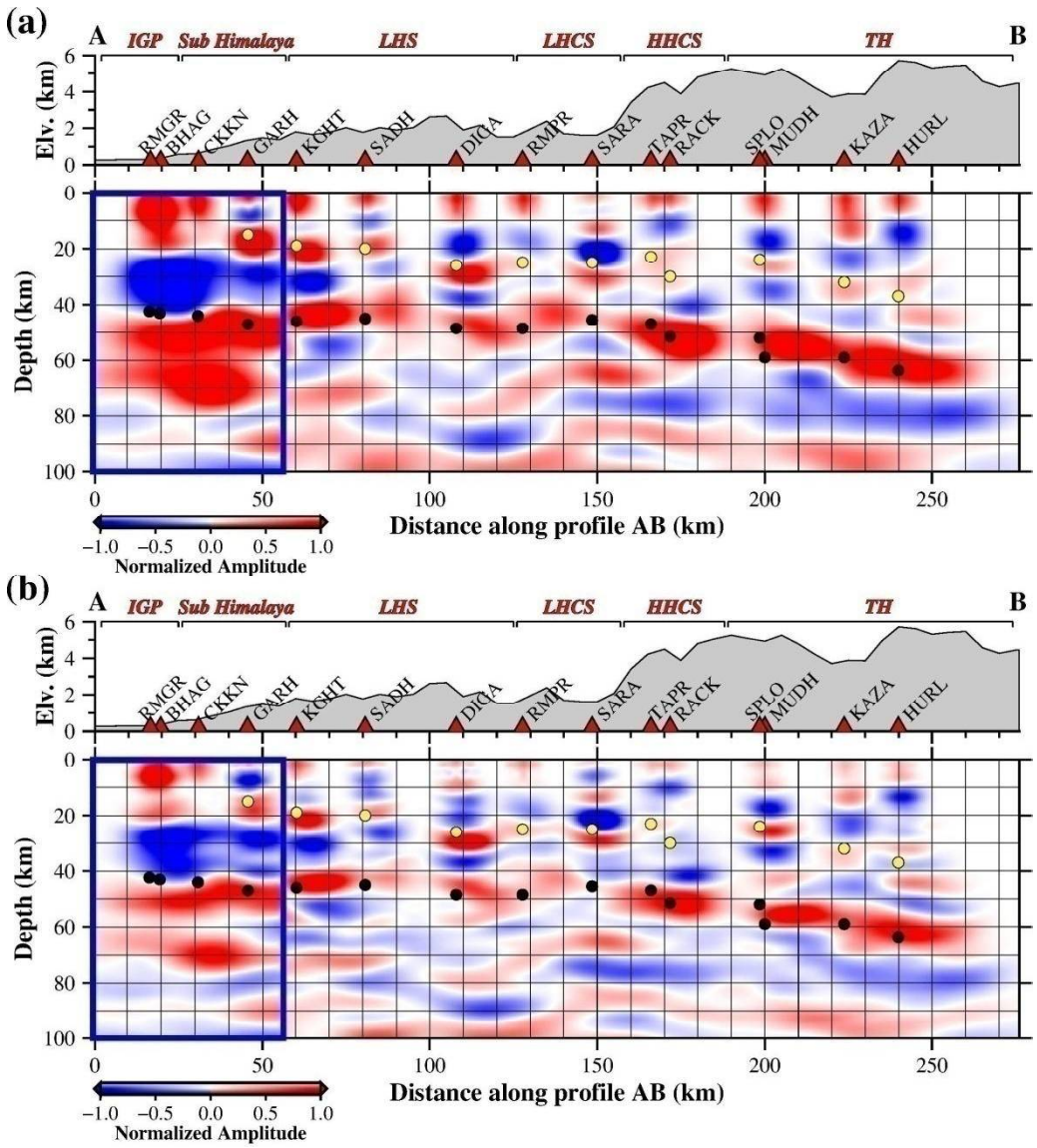

Figure 4.12 The Common Conversion Point depth migrated RF image for two different frequencies with Gaussian widths (a) 2.0 and (b) 5.0 along the A-B profile (Fig. 4.1). The consistent positive polarity shown by red signals of CCP image as well as projectedMoho depths estimated by NA inversion (black dots) and the MHT obtained by NA method is shown by yellow dots.

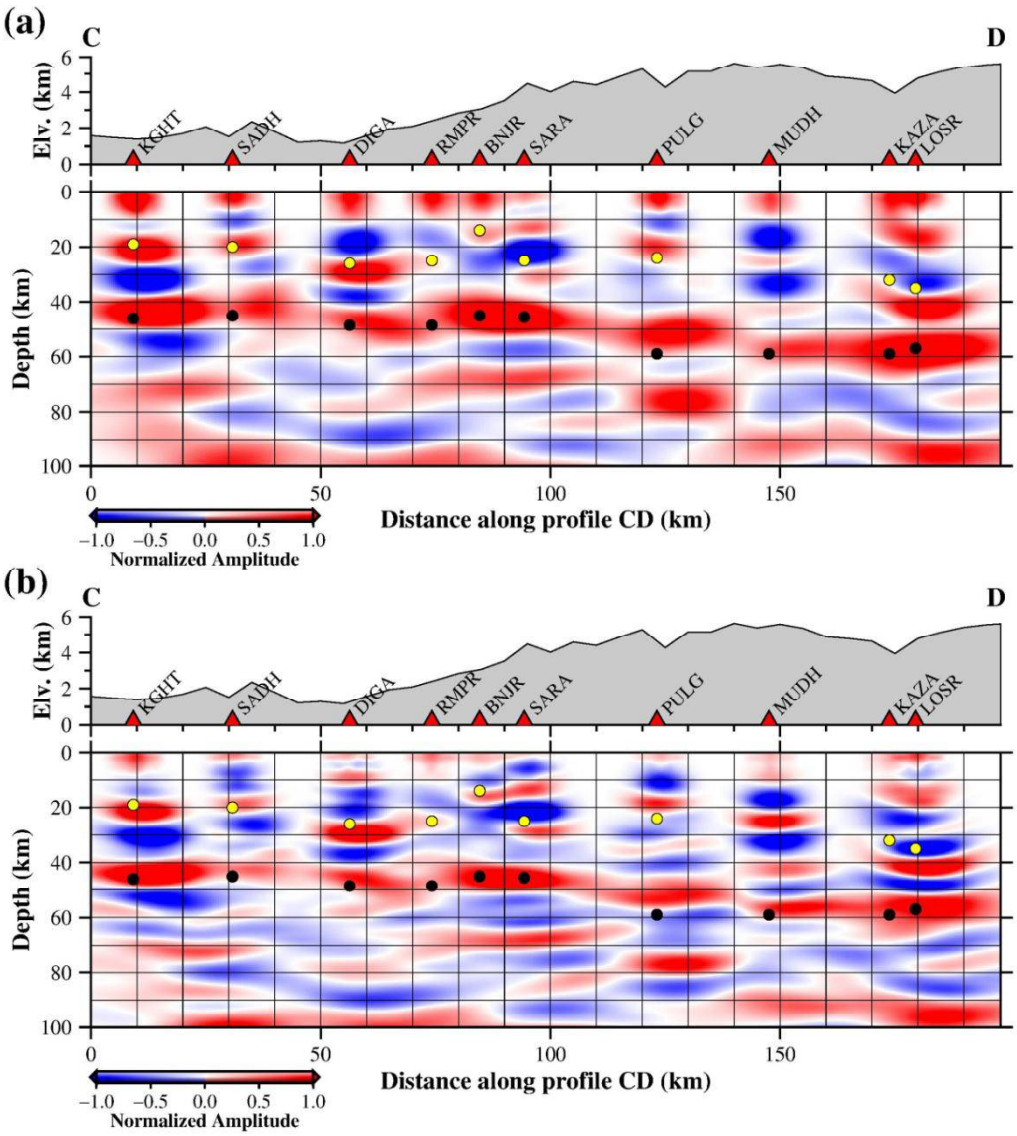

Figure 4.13 The Common conversion point depth migrated RF image for two different frequencies with Gaussian width (a) 2.0 and (b) 5.0 along the C-D profile (Fig. 4.1). The consistent positive polarity shown by red signal of CCP image as well as projected Moho depths estimated by NA method (shown by black dots) and the MHT is shown by yellow dots show good agreement with each other from KGHT to LOSR along the C-D profile irrespective of frequency used.

Both the CCP images and the inverted velocity models, reveal that depth of the MHT varies between ~16 km below the Sub-Himalaya and ~27 km below the Higher Himalaya indicating a gentle north dipping nature of the MHT in the study area (Figs. 4.12 and 4.13). However, a considerable change in depth of the MHT is observed from SPLO to HURL within a distance of ~50 km in the TH. The depth of the MHT is ~22 - 27 km near the STD (e.g. below SPLO and RACK), and it is ~38 km below the HURL station (Fig. 4.11). This abrupt increase in depth of the MHT suggests presence of a ramp structure on the MHT below the TH, which is further north (at a distance of about 180 km from the HFT) compared to that reported in other parts of the Himalaya (Pandey et al., 1995; Caldwell et al., 2013). Along ~150 km long segment of the profile, from RMGR to TAPR, the Moho depth varies from ~43 km at RMGR to ~46 km at TAPR. On the other hand, the change in crustal thickness is much significant (~15 km) from TAPR to HURL stations, which are located ~75 km apart. A cross-section of inferred geometry of the MHT and Moho along the A-B profile (Fig. 4.1) with different litho-tectonic units is shown in Figure 4.14.

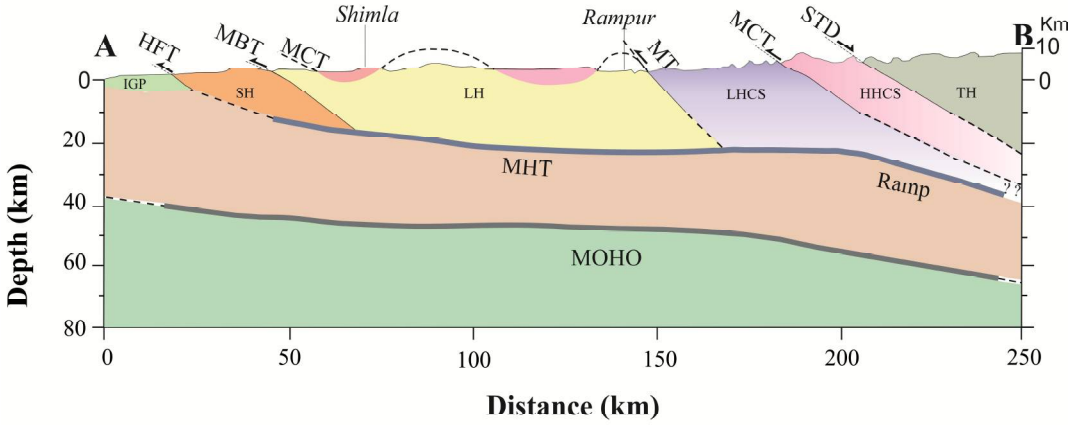

Figure 4.14 A cross section along the A-B transect marked in Fig. 5.1 with different litho-tectonic units indicating the gently dipping MHT a ramp beyond the STD and gradual dipping of the Moho from south to north.

4.4 DISCUSSION

4.4.1. VARIATION OF MOHO DEPTHS

The Moho discontinuity is recognized as the most significant and laterally continuous interface beneath the study profile. Three methods have been adopted (e.g. *H-k* stacking, NA inversion and CCP stacking) for estimating the depth of Moho or thickness of the crust beneath the stations of the study profile. All these methods show comparable results. The results from H-*k* stacking provide preliminary information regarding the estimation of average crustal thickness beneath a recording site. However, this method has some limitations and can be applied only to those RF data that clearly shows *Ps* phase and its crustal multiples. In deformation region like the Himalaya, it is intricate to identify the crustal multiple phases in the waveform data arriving from different azimuths. The application of H-*k* stacking to RFs of a particular narrow bin of BAZ and Δ may produce biased results as slowness for earthquakes with different distances differs significantly. This method could not be applied to RF data of BHAG, RMGR, and CKKN stations, however, the results obtained from other nine stations e.g. GARH, KGHT, SADH, DIGA, SARA, RACK, TAPR, SPLO, and HURL are in conformity with the results from NA inversions.

The inferred Moho depths obtained from NA inversions are marked in the CCP images by black filled circles in Figures 4.12 and 4.13. In most of the stations, both results from NA inversion and CCP stacking are similar. However, RMGR, BHAG and CKKN stations show different characteristics where the results from NA inversion slightly differ from CCP image. The individual RFs at these stations (Figs. 4.3*a* and 4.5) also shows characteristic differences with rest of the stations of the profile and has been discussed in section 4.3.2. The Moho phase is observed at ~7.0-8.0 s at stations near the HFT and the Sub-Himalaya (RMGR, BHAG and CKKN). This delayed arrival is due to the effect of sedimentary cover at these stations which leads to incorrect mapping of the Moho to much greater depth. This happens in CCP image as the method solely relay on the converted phases and plotting is done without accounting for the thick sedimentary layer. The NA inversion results,

however, shows the presence of thick sedimentary cover (~3-4 km) at the surface. In order to overcome the discrepancy observed in the CCP image beneath these stations, the shear wave velocity models obtained from NA inversion have been incorporated in the CCP stacking. The Moho depths thus inferred from all these methods suggest progressive deepening of Moho from the IGP to the TH. This northward dipping nature supports the fact that the Indian plate is under-thrusting towards the north. The average velocity in the crust estimated in this study is comparable with other studies carried out in the NW Himalaya by Rai et al. (2006) and Oreshin et al. (2008, 2011). The present day convergence rate in NW Himalaya as observed by GPS studies (Bilham et al., 1997; Banerjee & Burgmann, 2002) as well as the progressive dipping of Moho, provides support to the underthrusting mechanism (Ni & Barazangi, 1984).

4.4.2. VARIATION OF POISSON'S RATIO

The values of *Vp/Vs* and Poisson's ratio (σ), obtained from H-*k* stacking method at nine stations, show significant variation from south to north along the profile. Based on the fact that the average Poisson's ratio of the crust provides an idea of underlying rock types and mineral composition (Christensen & Fountain, 1975; Zandt & Ammon, 1995), it is tried to correlate with local geology and rock type beneath the seismological stations along with the laboratory estimates for common rock types reported by Christensen, (1996). The values of Poisson's ratio not only depends on rock type and mineral composition but also is influenced by fluid / partial melt present in the crust (O'Connell & Budiansky, 1974; Owens & Zandt, 1997; Wang et al., 2010). The Poisson's ratio is observed to be low for felsic rocks with high silica content and high for mafic rocks (Christensen, 1996).

The results from H-*k* stacking analysis indicates that Poisson's ratio values are largely related to the thickness of the crust and composition of the Himalayan wedge (sedimentary, metamorphic and igneous components) and subducting Indian crust. Influence of Indian crust is maximum at the southern end and it gradually decreases towards north as the thickness of Himalayan

orogenic pile increases. The result at GARH station shows a slightly lower value of *Vp/Vs*: 1.73 and σ: 0.249 compared to average values (*Vp/Vs* ~1.75, σ: 0.25) for the Indian crust (Singh et al., 2015). The main lithology near this seismological station is sandstone and shale (Dubey & Bhat, 1991). The laboratory estimates suggest a wide range of *Vp/Vs* values (~1.5-1.9) for sandstone, however, these values is minimum for unsaturated sandstone (*Vp/Vs* ~ 1.5) (McCormack et al., 1984). On the other hand, shale shows higher values (*Vp/Vs* ~ 2.43-2.70) (McCormack et al., 1984). Johnston & Christensen, (1995) also observed higher *Vp/Vs* values (>1.90) for shale samples. Considering the above-reported values for sandstone and shale, it can be inferred that sandstone with high quartz content possibly influences *Vp/Vs* ratio of the crust beneath GARH station to a considerable extent.

The low values observed at KGHT and SADH (*Vp/Vs* ~ 1.70; σ: 0.235) and local geology suggests felsic composition of the crust beneath these stations. The main rock types surrounding these stations are sandstone, shale, quartzite, limestone with minor meta-volcanic. The low values are possibly due to the presence of quartzite. The Poisson's ratio of quartzite is extremely low (σ : 0.102) (Christenson, 1996). In contrast, *Vp/Vs* values for limestone ranges from 1.71 to 2.75. Similar low σ value (0.235) is also observed in the HHCS (at DIGA station) which is comprised of high-grade metamorphic gneisses with the thick sequence of amphibolites facies to migmatites paragneisses with minor metabasites.

The RMPR station located over the LKRW of LHCS shows extremely low value (*Vp/Vs*: 1.68; σ: 0.225). The main lithology in and around this station is basalt undergone low-grade greenschist metamorphism. Basalt occurs in an association of quartzite (Webb et al., 2007). The *Vp/Vs* ratio of basalt is normally higher than our observed value at this station (Christensen, 1996). The occurrence of quartzite in association with basalt is a possible reason for the extremely low value of σ at RMPR. Moreover, green-schist and amphibolites facies rocks show low value of *Vp/Vs* and σ (Christensen, 1996).

The TAPR and RACK stations show intermediate values of *Vp/Vs* and σ. The observation at TAPR station is in conformity with local geology. The

common lithology in and around this station is massive granitic augen gneiss with minor concordant metabasites of the LHCS commonly known as 'Wangtu gneiss' (Vannay & Grasemann, 1998). The RACK is located over the HHCS and the lithology near the station mainly consists of pelitic gneisses and granitic gneisses. Xenoliths of pelitic and mafic composition are sporadically distributed in these gneissic rocks (Miller et al., 2001, Thakur & Patel, 2012). The results obtained at these stations are similar with laboratory estimation for granite gneisses as observed by Christensen, (1996).

The high values of *Vp/Vs* and σ at SPLO station (*Vp/Vs*: 1.77; σ: 0.265) which is located over the TH can be explained based on composition. Low-grade pelitic rock with mineral assemblage: muscovite-chlorite-biotite-plagioclase-quartz is the main lithology around this station. The estimated values are in good agreement with the published value of low-grade pelitic rock (σ: 0.266; *Vp/Vs*: 1.77) (Christensen, 1996). On the other hand, the cause of extremely high value of σ observed at HURL (σ: 0.27) may be because of the occurrence of metamorphic fluid/ partial melt beneath the TH. The occurrence of the leucogranite supports the presence of metamorphic fluid beneath KHAB station. The MT survey (Arora et al., 2007) and seismological studies (Caldwell et al., 2009; Hazarika et al., 2013, 2014) also support the occurrence of a fluid phase or a partial melt at mid-crustal depths beneath the TH.

The results obtained in the present study are comparable with that of Hazarika et al. (2013). The present study profile is the southern extension of the profile of Hazarika et al. (2013, 2014) and facilitates in obtaining a complete trace of average crustal thickness and Poisson's ratio from Sub-Himalaya to Ladakh-Karakoram zone. Hazarika et al. (2013) estimated low and normal values of σ in Lesser and Higher Himalaya, high values in the Tethyan Himalaya and unusual high values in Ladakh-Karakoram zone. The high value of σ beneath Ladakh and the Tethyan Himalaya with intra-crustal low-velocity zone at mid-crustal depth was interpreted as because of the existence of fluid phase/partial melt (Caldwell et al., 2009; Hazarika et al., 2014). The present study provides a constraint towards the southern limit of

this partial melt zone. The low and intermediate value of σ at stations over the Sub, Lesser and Higher Himalaya suggests the absence of such significant partial melting to the south of the profile.

4.4.3. GEOMETRY OF THE MHT AND SEISMICITY

The inference of depth of the MHT using RF study depends on which seismic converted phase is used for its demonstration. Based on expected lithologies Caldwell et al. (2013) imaged the MHT which was characterized by complex polarity signature beneath the Garhwal Himalaya and inferred significant ramp structure in the MHT. The MHT which is a basal decollement separating the overlying Himalayan wedge from the underlying Indian crust is highly deformed compared to the underlying Indian crust. Moreover, fluid expelled from underthrust sedimentary rocks is trapped above the MHT causing IC-LVL at shallow depth observed at some stations of the Sub, Lesser, and Higher Himalaya. On the other hand, the presence of partial melt and/or aqueous fluid is inferred for the generation of IC-LVL and high *Vp/Vs* ratio at greater depths in the TH (e.g. HURL station). Consequently, the base of the IC-LVL is considered as the MHT. The positive arrival at 4-5 s observed at the stations over the TH (MUDH, KAZA, and SPLO) is considered as the MHT which corresponds to step jump in velocity at 30-38 km depth. The positive phase arrivals at ~2-3 s at MUDH, KAZA, and SPLO indicate the presence of a shallow feature which may be the base of the Tethyan sediments. In all probabilities, this positive arrival prior to that of the MHT marks the contact between the Tethyan sedimentary rocks with the underlying crystalline of the Paleozoic basement of continental margin of northern India. The depth of the MHT obtained in this study is comparable with other observations reported near our study profile (Thakur et al., 2000; Chamoli et al. 2011; Caldwell et al., 2013). However, this study reveals gentle northward dipping structure of the MHT between the Sub and Higher Himalaya unlike ramp structure as reported in the Garhwal Himalaya (Caldwell et al., 2013) and central part of Nepal Himalaya (Pandey et al., 1995; Lavé & Avouac, 2001). Instead, ramp structure is identified further north of the profile beneath the TH

(Figs. 4.12 and 4.14). The geometry of MHT observed in the Satluj valley and other studies reported in the Garhwal and Nepal Himalayas (Pandey et al., 1995; Caldwell et al., 2013) suggest significant along-strike variation of the MHT in the Himalaya.

Several recent studies (e.g. Robert et al., 2011; Arora et al., 2012) have been reported the along-strike variation in the geometry of MHT, specifically the occurrence/non-occurrence of a major crustal scale ramp. The occurrence of mid-crustal ramp in the central Nepal region persuades the development of a sharp topographic shift, whereas both the ramp and topographic shift are inexistent in the Bhutan Himalaya (Robert et al., 2011). Although it is not straight forward to correlate topographic variation with subsurface structures, the topography between the Satluj valley profile and the Garhwal Himalaya seismic profile of Caldwell et al. (2013) are compared and shown in Figure 4.15. About 30 km wide and 220 km long swath averaged minimum, mean, and maximum elevation profiles have been generated using SRTM DEM data of 30 m resolution (https://earthexplorer.usgs.gov) along $AA^{/}$ profile of the present study and $BB^{/}$ profile of Caldwell et al. (2013) (Fig. 4.15*a*). Comparison of elevation profiles (Figs. 4.15*b*, *c*)indicates a sharp change in topography near the MCT (MT) in the $BB^{/}$ profile just above the mid-crustal ramp reported by Caldwell et al. (2013) which is not prominent in $AA^{/}$ profile. The absence of both ramp structure and topographic transition near MCT (MT) in Satluj valley highlight the significance of inherited relation between the geometry of the crust and the associated kinematics in laying the topography.The subsurface structure in the Himalayan region is controlled by the topographic ridges on the down-going Indian plate and the rifts and nappes in the overriding wedge of the Himalaya(Gahalaut & Kundu, 2012; Arora et al., 2012). Underthrusting of bathymetric features like DHR (Sastri et al., 1971; Valdiya, 1976; Karunakaran& Ranga Rao, 1979; Raiverman, 2002) (Fig. 4.1) can change the crustal configuration and geometry of the MHT as observed in this study. Rosenbaum and Mo, (2011) observed that the ridge structures responsible for the spatial distribution and frequency of the occurrence of earthquakes. A recent study using gravity anomaly data by

Hetenyi et al. (2016) reported lateral segmentation of subsurface structure in the Bhutan Himalaya.

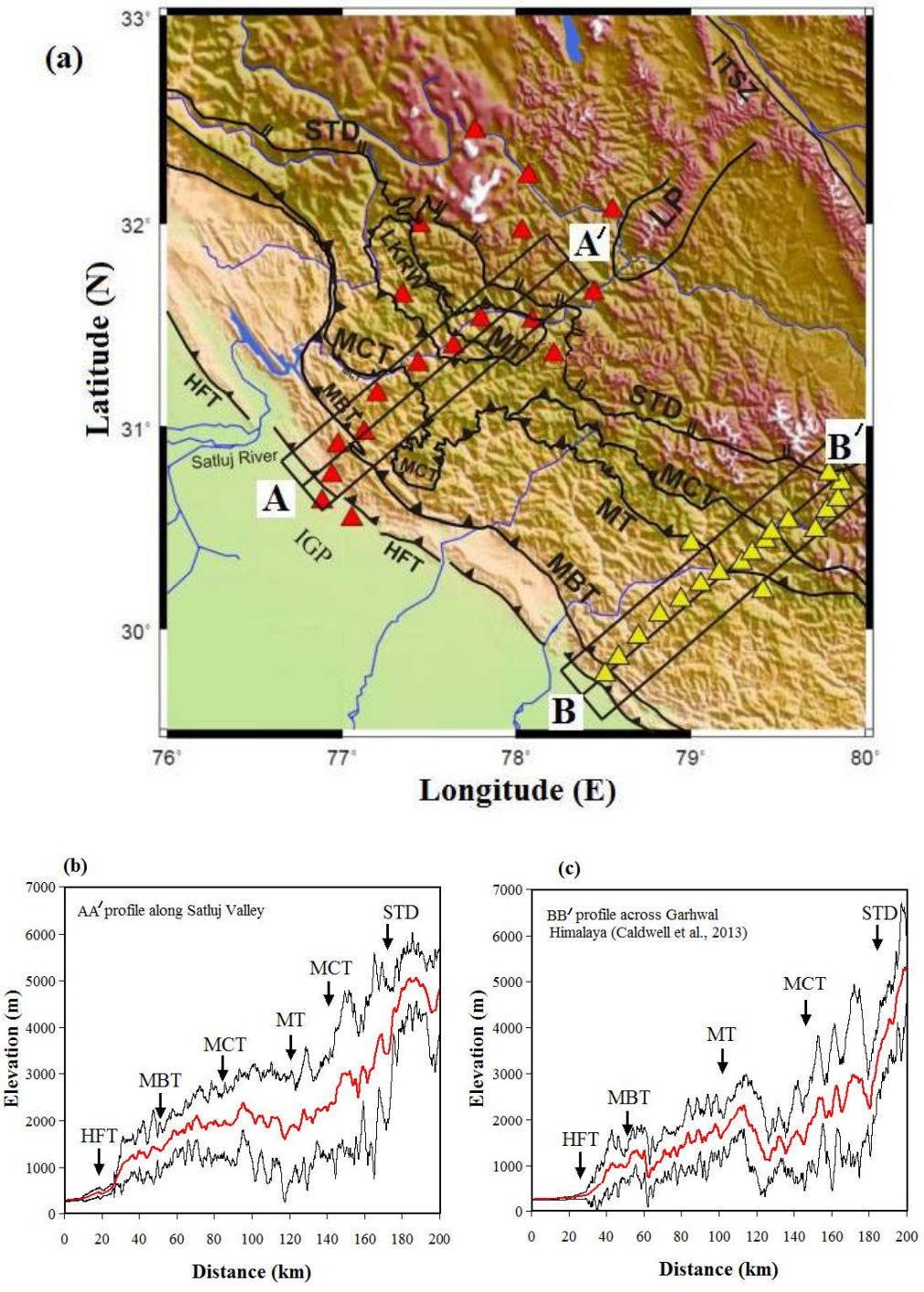

Figure 4.15(a) Topographic map with tectonic features as described in Figure 4.1, showing two seismological profiles AA/ (present study) and BB/ (Caldwell et al. 2013). About 25 km wide and 220 km long swath averaged minimum, mean, and maximum elevation profiles

obtained using SRTM DEM data (30 m resolution) along AA/ and BB/ profiles as shown in (b) and (c), respectively.

The spatial distribution of local earthquakes ($M \geq 3.0$) occurred during 1964 - April, 2017 has been analyzed in and around Satluj valley (Fig. 4.16). The detail information of hypocentral parameters of local earthquakes has been obtained from International Seismological Centre (ISC, www.isc.ac.uk) catalog. The observed pattern of seismicity shows three different zones namely Kangra-Chamba region, Satluj valley and the Garhwal Himalaya (Fig. 4.16). It is observed that moderate and large magnitude earthquakes are very less in the HSB segment of the southern end of Satluj valley (Shimla region) as compared to Kangra-Chamba region and the Garhwal Himalaya. The rapid migration or shift of seismicity in this segment is observed to the north near STD, at the Kaurik Chango Fault (KCF) zone. The cause of northward migration of seismicity is the effect of arc-perpendicular continuation of DHR structure in Himalayan foreland basin. This part of HSB is situated in the west of DHR and in the east of rupture zone of great 1905 Kangra earthquake of M8.0 (Middlemiss, 1910; Ambraseys & Bilham, 2000) (Fig. 4.16). It is reported that the seismicity in the HSB is mainly correlated with the ramp structure in the MHT (Pandey et al., 1995; Caldwell et al., 2013).

The pattern of seismicity in the HSB in Satluj valley and in adjacent Garhwal Himalaya clearly reflects the role of the ramp structure on the MHT in the generation of clustered seismicity (Caldwell et al., 2013). Several studies such as Avouac et al. (1992, 1993) and Farias et al. (2010) reported the relation between the occurrence of earthquakes and crustal ramp structure. The 1906 great earthquake of M8.3 occurred in Tien Shan mountain belt was observed to be related to the deep basement ramp structure (Avouac et al., 1993). Along the Andean margin, the ramp-flat detachment structure is considered to be the main cause of distribution of seismicity in this region (Farias et al., 2010). Similar type of studies has also been observed where crustal ramp structure is main causing factor of seismicity in the Alps and the San Gabriel mountains in California (Avouac et al., 1992, 1993).

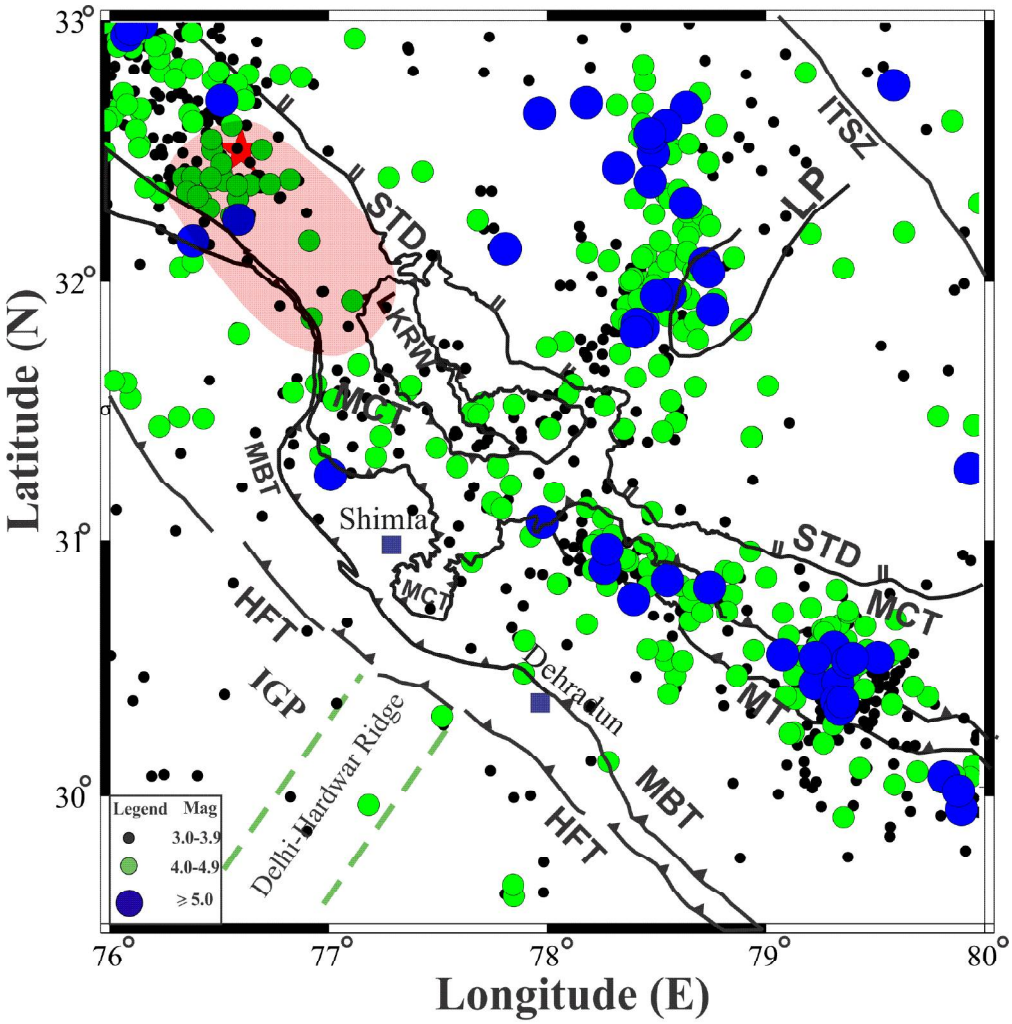

Figure 4.16 Distribution of earthquakes (M > 3.0) in the NW Himalaya for the period of 1960 – April, 2017 are shown in relation to major tectonic features existing in the region. The tectonic features are same as mentioned in Figure 4.1. The red star indicates epicenter of 1905 Kangra earthquake (Middlemiss 1910; Ambraseys & Bilham, 2000) and the shaded area shows the rupture area of 1905 Kangra earthquake modified after Wallace et al. (2005).

4.4.4 CAUSE OF S-LVL AND IC-LVL

The S-LVL beneath BHAG, RMGR, CKKN and GARH is observed due to the presence of a 3-4 km thick sequence of a sedimentary column in the IGP and the Sub-Himalaya. Several seismological studies reported the surface sedimentation in the IGP as the main cause of S-LVL (e.g. Hetényi et al.,

2006; Mitra et al., 2011; Srinivas et al., 2013 and Borah et al., 2015). The similar observation reported by Mitra et al. (2011) using surface wave analysis, measured the sedimentary thickness of the alluvium of the IGP. Rai et al. (2006) observed that the thickness of sedimentary column is 3.0-4.0 km in the IGP using joint inversion study of RF and surface waves. Besides the seismological studies, the borehole data can also provide an estimate of the depth of a sedimentary basin. A number of borehole wells were drilled in the nearby region of study area out of which Adampur well drilled in the alluvium of IGP from which it was observed that the thickness of Siwalik sediments over the granitic basement is 2513 m (Rao, 1973).

The stations located to the north of the Sub Himalaya e.g. KGHT, DIGA, BNJR, PULG, RMPR, TAPR, and RACK show the characteristics of IC-LVL at shallow depth. Several studies reported that an IC-LVL is attributed to partial melt/aqueous fluid (Nelson et al., 1996; Klemperer, 2006; Caldwell et al., 2013). As the mechanism of partial melting is not sustainable at shallow depth, the possible cause of IC-LVL at shallow upper crust is explained by the presence of trapped fluid expelled from the under-thrusting sedimentary rocks (Hyndman & Shearer, 1989; Jones, 1992; Litvinovsky et al., 2000; Nabelek et al., 2009).

The occurrence of the IC-LVL at 25-38 km beneath HURL station in the TH, as observed in this study, is possibly related to a temperature controlled dehydration reaction which gave rise to the liberation of a partial melt or a metamorphic fluid (Hyndman & Shearer, 1989; Jones, 1992). A number of studies carried out in the Tibetan Plateau (Nelson et al., 1996; Schulte-Pelkum et al., 2005; Klemperer, 2006; Xu et al., 2007; Lemonnier et al., 1999; Duputel et al., 2016) as well as in different litho-tectonic units of the Himalaya (Caldwell et al., 2009; Hazarika et al., 2014) suggested the presence of IC-LVL. The existence of aqueous fluid/ partial melt detected at mid-crustal depth has also been supported by low resistivity anomaly observed in MT studies carried out in the Tibetan Plateau and in the NW Himalaya (Unsworth et al., 2005, Arora et al., 2007).